2009

Experimental Study of Synthetic Jets

Hoda Eiliat
University of Windsor

Recommended Citation

Eiliat, Hoda, "Experimental Study of Synthetic Jets" (2009). *Electronic Theses and Dissertations.* Paper 183.

EXPERIMENTAL STUDY OF SYNTHETIC JETS

by

Hoda Eiliat

A Thesis

Submitted to the Faculty of Graduate Studies through

Mechanical, Automotive and Materials Engineering

in Partial Fulfillment of the Requirements for

the Degree of Master of Applied Science at the

University of Windsor

Windsor, Ontario, Canada

2009

Experimental Study of Synthetic Jets

by

HODA EILIAT

APPROVED BY:

Dr. X. Nie, External Department Reader
Mechanical, Automotive and Materials Engineering

Dr. D. Ting, Department Reader
Mechanical, Automotive and Materials Engineering

Dr. G. W. Rankin, Advisor
Mechanical, Automotive and Materials Engineering

Dr. A. Fartaj, Co-Advisor
Mechanical, Automotive and Materials Engineering

Dr. V. Stoilov, Chair of Defense
Mechanical, Automotive and Materials Engineering

14 May 2009

Author's Declaration of Originality

I hereby certify that I am the sole author of this thesis and that no part of this thesis has been published or submitted for publication.

I certify that, to the best of my knowledge, my thesis does not infringe upon anyone's copyright nor violate any proprietary rights and that any ideas, techniques, quotations, or any other material from the work of other people included in my thesis, published or otherwise, are fully acknowledged in accordance with the standard referencing practices. Furthermore, to the extent that I have included copyrighted material that surpasses the bounds of fair dealing within the meaning of the Canada Copyright Act, I certify that I have obtained a written permission from the copyright owner(s) to include such material(s) in my thesis and have included copies of such copyright clearances to my appendix.

I declare that this is a true copy of my thesis, including any final revisions, as approved by my thesis committee and the Graduate Studies office, and that this thesis has not been submitted for a higher degree to any other University or Institution.

ABSTRACT

An experimental investigation on the mean velocity distribution of a round synthetic jet generated by an acoustic driver has been performed and analyzed. Velocity profiles at the orifice plane and at parallel planes located at various distances have been obtained for this purpose. The main objective of this thesis is to determine the effect of orifice diameter and jet excitation frequency using dimensionless parameters (Reynolds number and Stroke Length) on the velocity profiles of synthetic jets. Results obtained from the experimental analysis are compared to the existing results and the trends are in good agreement.

Dedicated to:

My country, Iran

My Mother, Mina

And

My Husband, Mohammad

ACKNOWLEDGEMENTS

I thank God for giving me the power to follow my way to discover the unknowns and for sending me an angel, my mother who first instilled a sense of wonder and a love of learning in me. I would like to express my deep appreciation to my husband, Mohammad for his unconditional love, consideration and understanding.

I would like to extend my gratitude to my advisor Dr. Rankin for his support and patience during the conduct of these experiments. His direct supervision and guidance for establishing the experimental setup is appreciated. I also would like to thank Dr. Fartaj for reviewing the work throughout the process and for his suggestions. Without the generous help of my advisors, this investigation would not have been possible.

I would like to express my sincere thanks to my thesis committee members Dr. D. Ting and Dr. X. Nie. I would also like to express my thanks to Patrick Seguin for his generous help with my experiment setup.

Lastly, I would like to thank my colleagues and everyone who shared a part of their time and knowledge in the accomplishment of this thesis.

TABLE OF CONTENTS

AUTHOR'S DECLARATION OF ORIGINALITY................................ iii

ABSTRACT...iv

DEDICATION v

ACKNOWLEDGEMENTS vi

LIST OF TABLES...x

LIST OF FIGURES..xi

NOMENCLATURE xv

INTRODUCTION 1

1.1 Synthetic Jets 1

1.2 Synthetic Jet Scaling Parameters...3

1.2.1 Dimensionless Stroke Length..3

1.2.2 Dimensionless Velocity Scale..5

1.2.3 Reynolds Number...7

1.3 Thesis Outline...8

LITERATURE SURVEY AND OBJECTIVES 10

2.1 General Work (Applications) 10

2.2 Experimental Studies..13

2.3 Objectives 23

EXPERIMENTAL METHODOLOGY 25

3.1 Experiment Apparatus 25

3.1.1 Synthetic Jet Device 27

3.1.2 Signal Generating Equipment 28

3.1.3 Traverse Equipment 29

3.1.4 Hot-wire Anemometry 30

3.2 Experimental Procedure 37

3.2.1 Data Acquisition...39

3.3 Data Processing 41

RESULTS AND DISCUSSION..47

4.1 Orifice Exit Plane Study..47

4.2 Synthetic Jet Centerline Study...52

4.3 Velocity Profiles in the Radial Direction Study..............................55

CONCLUSIONS AND RECOMMENDATIONS 58

5.1 Conclusions 58

5.2 Recommendations 59

APPENDICES..60

Appendix A: Uncertainty Analysis 60

A.1 Bias in Velocity..61

A.2 Precision in Velocity 65

A.3 Velocity Uncertainty 68

A.4 Diameter Measurement Uncertainty 68

A.5 Frequency Measurement Uncertainty 69

A.6 Input Signal Voltage Measurement Uncertainty................70

A.7 U_{bar} and U_o Uncertainty 71

A.8 Uncertainty in Traverse Positioning....................................73

A.9 Uncertainty in U/U_{cl} 73

A.10 Uncertainty in r/d...74

A.11 Uncertainty in b/d..75

B.1 Hot-wire Anemometry Calibration Procedure 76

B.2 Hot-wire Anemometry Measurement Procedure................84

B.3 Hot-wire Anemometry Post Analysis.................................89

Appendix C: Data Obtained From the Measurements 91

REFERENCES...92

VITA AUCTORIS 97

LIST OF TABLES

Table 1 Synthetic jet device specification parameters. 28

Table 2 Specification of the probe, adopted from TSI, IFA300 probe box. 32

Table 3 Probe positions on the orifice plane and U_{bar}/U_o values for 10 mm diameter at 10 Hz. 48

Table 4 Probe positions on the orifice plane and U_{bar}/U_o values for 10 mm diameter at 20 Hz. 49

Table 5 Probe positions on the orifice plane and U_{bar}/U_o values for 15 mm diameter at 10 Hz. 50

Table 6 Probe positions on the orifice plane and U_{bar}/U_o values for 15 mm diameter at 20 Hz. 51

Table 7 U_o values at center of the orifice...52

Table 8 Uncertainty analysis results. 70

LIST OF FIGURES

Figure 1 The schematic of a typical synthetic jet device. 2

Figure 2 The value of U_o and U_{bar}, area A or B is U_o and area A+B is U_{bar}. 7

Figure 3 Effect of Reynolds number and orifice height-to-diameter aspect ratio on synthetic jet formation. Adopted from Holman [4]. 18

Figure 4 Flow regions as a function of Reynolds number: (a) laminar jet, (b) laminar rings, (c) transitional jet, (d) turbulent jet [30]. 21

Figure 5 Different geometries: a) cylindrical, b) pitched and c) clustered.22

Figure 6 Orifice plate cross-sections used by Shuster and Smith: (a) straight, (b) beveled, (c) rounded [6]..23

Figure 7 Block diagram of experiment setup. 26

Figure 8 Hot-wire Anemometry, calibrator and computer. 26

Figure 9 Synthetic jet device, signal generating and traverse equipment.27

Figure 10 Detailed schematic of synthetic jet dimensional parameters. ..29

Figure 11 A schematic of the traverse location, hot-wire and synthetic jet device. 30

Figure 12 Calibration curve fitted by a polynomial 5th order curve. 33

Figure 13 Connection between IFA300, air calibrator, pressure transducer, A/D board and computer [36]...35

Figure 14 A/D board connections with function generator and IFA300..36

Figure 15 Effect of directional ambiguity on the output signal. 37

Figure 16 U_{bar}/U_o versus number of sampling points.............................39

Figure 17 Measurement points at the orifice plate......................................40

Figure 18 Measurement points along the centerline of the jet exit...........40

Figure 19 Measurement points at d/2 and 11d/4 axial distances, perpendicular to the jet axis. 41

Figure 20 Ejection and suction phase along the centerline at X=0, X=d/2 and X=d/4. 42

Figure 21 All 33 measurement cycles layered on one period for the 10 mm-10 Hz jet. 43

Figure 22 Fourier series. 44

Figure 23 Reversing the suction cycle by using Fourier series and the minimum point...46

Figure 24 3D plot at the orifice plane for 10mm diameter and 10 Hz frequency. 48

Figure 25 3D plot at the orifice plane for 10mm diameter and 20 Hz frequency. 49

Figure 26 3D plot at the orifice plane for 15mm diameter and 10 Hz frequency. 50

Figure 27 3D plot at the orifice plane for 15mm diameter and 20 Hz frequency. 51

Figure 28 Time-averaged centerline velocity versus downstream distance from 0 to 3d with d/4 steps. 53

Figure 29 Smith and Swift results for time averaged centerline velocity versus downstream distances [1]. 54

Figure 30 Experimental results, time averaged centerline velocity versus downstream distance (Log scale)..55

Figure 31 Mean velocity profile taken at d/2 distance downstream. 56

Figure 32 Mean velocity profile taken at 11d/4 distances downstream. ..56

Figure 33 Jet width based on half maximum velocity as a function of downstream distance. 57

Figure 34 Misalignment degree (θ). 63

Figure 35 Phase locked data and Fourier fitted curve for 10-10-0-0........66

Figure 36 Velocity values at t=0 and t= $T/2$ for 10-10-0-0. 66

Figure 37 Automated air calibrator used to calibrate the probe [36]. 77

Figure 38 Calibration-probe data screen. 78

Figure 39 Gain and offset calculator..80

Figure 40 Calibration-data table...81

Figure 41 Calibration-condition setup...82

Figure 42 Acquired calibration points..83

Figure 43 Calibration curve fitting screen...84

Figure 44 Traverse control table..85

Figure 45 Acquisition-probe data. 86

Figure 46 Acquisition-condition setup..87

Figure 47 File name and definition of each section. 87

Figure 48 Triggering temperature requirement......................................88

Figure 49 Input signal and synthetic jet velocity graph..........................89

Figure 50 Post analysis. 90

NOMENCLATURE

$\boldsymbol{a}$	speed of sound
$\boldsymbol{a_o}$	speed of sound at stagnation condition
A	cross-sectional area of the neck
b	jet width (centerline location where velocity is 0.5 U_{Cal})
B	bias error
$\mathbf{C_V}$	calibration velocity
D	diameter of the orifice
$\boldsymbol{F}$	frequency of oscillation
h	orifice slot height
H	distance between jet’s orifice and heated surface
L	length of the chamber
$\boldsymbol{L_o}$	Stroke Length
$\boldsymbol{M}$	number of cycles in velocity measurement
Ma	Mach number
N	number of data points in each cycle
P	precision error
$\boldsymbol{P_o}$	standard pressure
$\boldsymbol{P_t}$	total pressure
R	radius curvature
$\boldsymbol{Re_{Uo}}$	Reynolds number of synthetic jet

St	Strouhal number
t	Time
T	driving period
$\mathbf{T}^{\circ}$	temperature
$\bar{\boldsymbol{T}}$	averaged(mean) period over the number of cycles
U	time-averaged velocity
$\boldsymbol{U}_{\boldsymbol{ave}}$	average velocity for a continuous jet
$\boldsymbol{U}_{\boldsymbol{Cal}}$	calibration velocity
$\boldsymbol{U}_{\boldsymbol{cl}}$	centerline velocity
$\boldsymbol{U}_{\boldsymbol{o}}$	downstream-directed velocity during half of the cycle averaged over the full cycle
$\boldsymbol{u}_{\boldsymbol{o}}(\boldsymbol{t})$	centerline velocity as a function of time
$\boldsymbol{u}_{\boldsymbol{max}}$	maximum of $u_o(t)$
V	volume of the cavity
X	downstream distance
Y	stream wise coordinates
Z	stream wise coordinates

Greek Letters

$\boldsymbol{\gamma}$	ratio of specific heat (C_P/C_V)
$\boldsymbol{\Delta P}$	differential pressure

ΔT	difference between ambient reference temperature and the temperature during the measurements
θ	degree of misalignment
ϑ	speed of sound in air
λ	mean free path
μ	dynamic viscosity
ν	degree of freedom
ρ	density of air
σ	particle diameter
ω	angular frequency

Abbreviations

CTA	Constant Temperature Anemometer
LDA	Laser Doppler Anemometer
PIV	Particle Image Velocimetry
STD	Standard Deviation
ZNMF	Zero-Net-Mass-Flux

Chapter 1

INTRODUCTION

This chapter presents general information on synthetic jet devices. Section 1.1 includes the definition of synthetic jet. Parameter scaling and velocity scaling of synthetic jets are explained briefly in Sections 1.2 and 1.3. The chapter concludes with the outline of the thesis contents.

1.1 Synthetic Jets

Synthetic jets have recently received a lot of attention both experimentally and numerically in connection with many applications. These jets can be formed in different ranges of length and time-scales and can be used in many flow control applications. They are considered as an excellent replacement for fans in different applications such as cooling electronic devices. Unlike conventional jets, synthetic jets are known to have a unique feature which is Zero-Net-Mass-Flux. This advantage makes it unnecessary to use any flow source since these jets have the ability to direct airflow with finite momentum and no additive mass [1].

A typical synthetic jet consists of three main parts: orifice, chamber and driver (Figure 1)

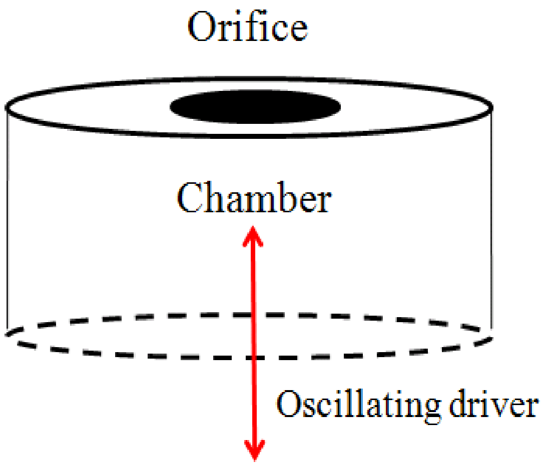

Figure 1 The schematic of a typical synthetic jet device.

Orifice diameter can affect the mean velocity of the synthetic jet. Utturkar [2] did a numerical study on sensitivity of the synthetic jet to the design of the orifice by using different aspect ratios. Orifice radius can affect the extent of flow separation from the edges of the orifice and therefore the velocity profiles. Chamber volume size determines the natural frequency of the device. The Helmholtz resonance model is a quantitative explanation of the air mass motion and momentum in the chamber and will be more fully explained in Section 3.3. The driver plays an important role in formation of synthetic jet as it determines the jet strength and frequency. Piezoelectrical [3, 4], acoustical [5] and mechanical (pistons) [6] drivers have been used.

The term “Synthetic Jet” was defined by Smith and Glezer [7] as a time-averaged flow motion which is generated by oscillatory flow at a sudden expansion. In order to explain the formation of a synthetic jet two phases can be defined: Ejection and Suction. A synthetic jet is produced by the interaction of a series of vortices which are formed by sudden alternation of the two phases of the flow across the orifice. During suction low pressure draws the flow into the chamber through the orifice followed by ejection, where the high pressure expels air from the chamber. Flow separates at the edges of the orifice and shapes a vortex ring which travels away from the orifice powered by its own self-induced velocity.

A synthetic jet takes the fluid from its surrounding and produces a jet with a forward velocity by transferring linear momentum to the flow without adding any mass flux across the system boundary. An oscillating flow with a zero time-averaged mean velocity through an orifice is needed to produce a synthetic jet flow. The oscillatory flow can be imposed by different kinds of driver. The oscillation amplitude should be large enough to cause the flow to separate at the orifice and induce the time-periodic rollup of the vortices. As the vortex rings move away from the orifice downstream, they are disturbed by the viscous effect, deformed and become similar to a steady turbulent jet.

1.2 Synthetic Jet Scaling Parameters

It is important to define relevant and meaningful parameters in order to compare and judge synthetic jet behavior. These parameters are usually derived from flow variables such as pressure, velocity and time. Each of these parameters is explained here briefly.

1.2.1 Dimensionless Stroke Length

Stroke Length quantifies the distance a particle on the jet centerline in the flow moves away from the orifice downstream. Smith and Swift [1] defined Stroke Length for a synthetic jet as:

$$L_o = \int_0^{T/2} u_o(t)\, dt \tag{1}$$

where $u_o(t)$ is the centerline velocity at X=0 for a synthetic jet, T/2 is half the period of the oscillation cycle and d is the diameter of the orifice. For a sinusoidal oscillation, Stroke Length can be modified as:

$$L_o = \int_O^{T/2} u_{max} sin(\omega\, t) dt \tag{2}$$

where u_{max} is the maximum velocity amplitude and it is assumed to be uniform over the orifice, ω is the angular frequency of oscillation and it is equal to ${}^{2\pi}/_{T}$. This integral can be evaluated and expressed in dimensionless form as:

$$\frac{L_o}{d} = \frac{u_{max}}{\pi f d} \tag{3}$$

knowing that the oscillating frequency is $f = {}^{\omega}/_{2\pi}$.

The dimensionless Stroke Length can be interpreted as a dimensionless frequency like Strouhal number. Strouhal number for an oscillating flow is defined as:

$$St = \frac{fd}{u_{max}} \tag{4}$$

The relation between dimensionless Stroke Length and Strouhal number is:

$$\frac{L_o}{d} = \frac{1}{\pi\, St} \tag{5}$$

Since Stroke Length is more meaningful physically as a gauge for displacement of the particle, Strouhal number is not used.

1.2.2 Dimensionless Velocity Scale

To determine the net effect over a whole cycle, defining a time averaged quantity is useful. Period averaged velocity is known as the time integral of the stream-wise velocity over a period, divided by a period as given below.

$$U_{bar} = \frac{1}{T}\int_0^T u_o(t)\, dt \tag{6}$$

$u_o(t)$ is the centerline velocity as a function of time at X=0 for a synthetic jet. In order to compare different synthetic jets, a velocity scale specifically for synthetic jets was defined by Smith and Swift [1] as follows:

$$U_o = L_o f = \frac{1}{T}\int_0^{\frac{T}{2}} u_o(t)dt \tag{7}$$

U_o is the downstream directed velocity of the flow only during the ejection phase of the synthetic jet (half of the oscillation cycle) and it is averaged over the whole period of the oscillation.

Figure 2 demonstrates one cycle of the data taken at X=0 for a 10 mm diameter orifice. The area under the curve for half of the cycle (U_o) is shown by A and for the next half of the cycle by B. U_{bar} at the exit plane of the jet is zero theoretically, since the suction and ejection values are the same (A-B=0). Moving away on the centerline downstream, ejection increases and suction decreases.

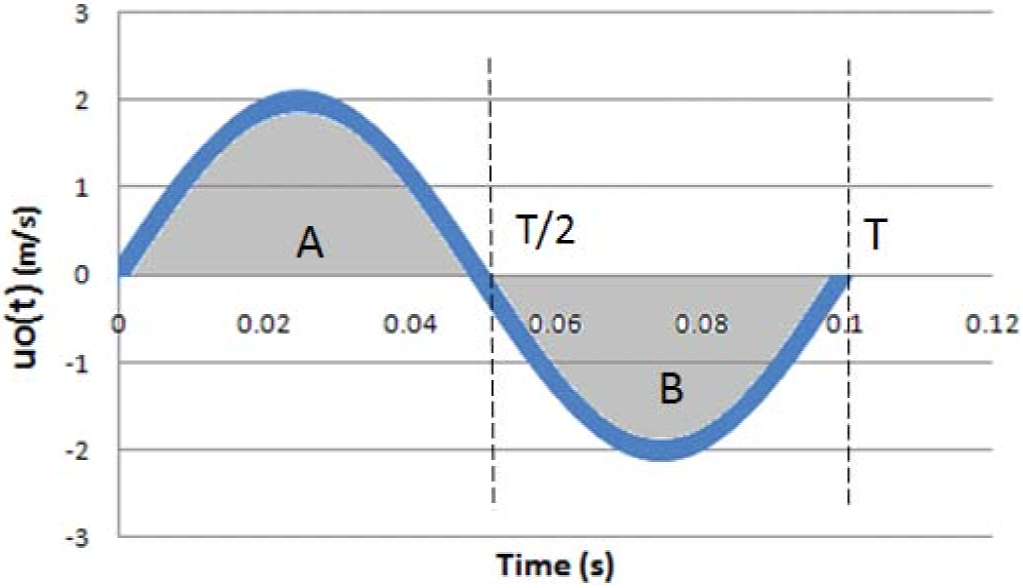

Figure 2 The value of U_o and U_{bar}, area A or B is U_o and area A+B is U_{bar}.

1.2.3 Reynolds Number

Reynolds Number is considered a useful parameter in defining jets, as it indicates the likelihood of turbulent flow. Based on the average downstream directed velocity during the ejection phase and the width of the channel, a commonly used Reynolds number in studying rectangular synthetic jets, is defined as below:

$$Re_{Uo} = \frac{U_o \ h}{\nu} \tag{8}$$

ν is the kinematic viscosity (dynamic viscosity divided by the density ($\nu = {}^{\mu}/_{\rho}$) and h is the width of the channel. For a round orifice, Reynolds number is modified as below, in which, d is the diameter of the orifice.

$$Re_{Uo} = \frac{U_o \ d}{\nu} \tag{9}$$

Another common definition for Reynolds number is based on the maximum velocity amplitude:

$$Re = \frac{u_{max} h}{\nu} \tag{10}$$

1.3 Thesis Outline

In this study, velocity profiles of a synthetic jet are measured using a hot-wire anemometer along the jet centerline at different distances from the orifice plane and also across various planes perpendicular to the jet axis. A round orifice was used and measurements were taken in air, at approximately 20° C and atmospheric pressure.

The outline of the thesis is as follows. Chapter 2 presents a brief description of the studies completed and published on synthetic jet formation, evaluation and applications. The experimental apparatus and measurement techniques are explained in Chapter 3. Chapter 4 describes the results of velocity measurements. Data reduction and analysis techniques applied to the results are also presented. Chapter 5 offers conclusions and recommendations. An uncertainty analysis of the measurements can be found in Appendix A, while Appendix B gives details of the hot-wire calibration process and measurement procedure. The data files obtained from the measurements and analyzed on spread sheets are collected on a CD-ROM attached to Appendix C.

Chapter 2

LITERATURE SURVEY AND OBJECTIVES

This chapter consists of three sections. Section 2.1 is a literature review of general work concerning synthetic jets. Some applications of synthetic jets are mentioned in this section. Since the current work was based on an experimental study, focus is more on experimental studies of synthetic jets. Section 2.2 presents experimental studies which have been carried on the formation, evaluation, near and far field evolution of the synthetic jets. Lastly, Section 2.3 includes thesis objectives.

2.1 General Work (Applications)

Aspects of formation, velocity profiles and applications of synthetic jets have been studied both experimentally and numerically in the last 40 years. They are also referred to as Zero-Net-Mass-Flux (ZNMF) devices due to their unique nature of a zero net mass injection across their system boundary. This makes them a desirable and affordable choice for a variety of applications such as flow control, fluid mixing, mass transfer, thermal management and cooling as indicated in the next paragraphs. Simplistic design is another attractive feature for industrial researchers to examine and explore the behavior of synthetic jets.

Different technical applications of synthetic jets have been investigated such as flow control applications like jet vectoring. Smith and Glezer [8] conducted an experimental study about the vectoring effect that a synthetic jet can have on a steady jet. Both jets had the same length but different aspect ratio. The aspect ratio of the synthetic jet orifice was 25 times larger than the steady jet. They were mounted on the same plane with 1.8 mm distance between them. The interaction between the steady jet and the synthetic jet was investigated using particle image velocimetry (PIV). It was shown that the steady jet flow is directed into the synthetic jet orifice and the interaction between the jets lead to the formation of a closed recirculation flow domain. They also studied the characteristic effect of vectoring angle on the deflection of the steady jet flow towards the synthetic jet [9]. Additional experimental and numerical investigations concerning jet vectoring can be found in Pack and Seifret [10] and Guo *et al* [11] respectively.

The effect of synthetic jet flows normal to the parallel flow of hot and cold streams was studied experimentally [12]. It was found that the degree of mixing was a function of jet actuation. What makes utilizing synthetic jets as a mixing aid attractive, is the lack of additional cold dilution air needed due to the ZNMF nature of the jet. The temperature distribution at 80 diameters downstream was measured in order to find the mixing efficiency of the jet. Mixing efficiency was found to be a function of the synthetic jet actuation. At low actuation, the distribution was not uniform since there was not enough mixing action. The temperature difference was from 40°C to 740°C. For high actuation, a more uniform distribution was observed.

Travenicek and Tesar [13] used an annular synthetic jet device to observe the mass transfer effect on the thickness of the Naphthalene layer, coated the surface. Two different flow fields were found by smoke visualization method in this study, “weak” and “strong”. These two fields were a function of oscillation amplitude. For the “strong” field the extent of mass transfer was greater than “weak” field.

A 2-D synthetic jet actuator in a rectangular channel with low flow rate was used in Mahalingam *et al* [14]. The effect of channel width on thermal efficiency and heat transfer coefficients were studied. It was found that thermal effectiveness of the jet actuator induced cooling in the channel, decreases with increasing channel width and increases with the temperature difference between the wall and the exit air. The study shows that the jet actuator demonstrates higher heat transfer at low flow rates. Mahalingam [15] in 2007 predicted thermal performance of synthetic jet by developing a model based on the solution of mass and momentum equations in a channel. The experimental results acquired in the previous study were also compared with the numerical predictions from the modeling.

In another study Campbell *et al* [16] used an electromagnetic driven synthetic micro-jet for cooling a laptop processor. A 22% reduction of mean temperature of the operating processor was obtained versus natural convection alone. Different variables such as actuation frequency, amplitude and geometry were used to determine an optimized synthetic jet.

A comparison study between synthetic jets and continuous jets regarding the cooling effects of a constant heat flux was conducted by Mahalingam [14]. High frequency synthetic jets (f =1200 Hz) were found to remove heat better than low frequency jets (f =420 Hz) for smaller H/d (H is the distance between jet’s orifice and heated surface). For larger H/d, an opposite relation was found. Synthetic jets were found to be three times more effective in cooling than continuous jets at the same Reynolds number.

The cooling performance of synthetic jets in a rectangular channel was also studied numerically in Mahaligam 2007 [15].

Amitay *et al* [17, 18] investigated a two-dimensional airfoil with a cylindrical portion of the leading-edge section fitted with a synthetic jet for flow separation control. For angles of attack greater than 5° and at a chord Reynolds number of 3×10^5, the flow separated from the airfoil surface. It was found that the location of the synthetic jets and their amplitude are critical to flow reattachment. Complete and partial reattachments occurred up to an angle of attack of 15° and 25°. The flow over an airfoil with a synthetic jet near the leading edge is numerically simulated by Ravindran [19], It was shown that for high angles of attack, increasing of the synthetic jet strength causes the lift coefficient to increase as well.

In another study Kiddy *et al* [20] worked on designing, modeling and fabricating micro synthetic jets to be used in flow control applications. They used miniature pressure tubes and observed velocities up to 20 m/s.

2.2 Experimental Studies

A Zero-Net-Mass-Flux jet flow was first observed by Ingard and Labate [21]. Their study included diameters of 3.5 mm to 20 mm and velocities of 0 m/s to 7 m/s. Acoustic waves were used to form the sinusoidal motion. They used stroboscopic illumination to characterize acoustic streaming through a circular orifice.

Medinkov and Novitskii [22] used an acoustically driven conical tube to observe the formation of Zero-Net-Mass-Flux jet from opposing trains of vortex rings on both sides of the orifice. By inducing frequencies from 10 to 100 Hz, they observed velocities up to 17 m/s.

Lebedeva [23] transmitted a high amplitude sound wave (500 to 1600 Hz) through an orifice of 0.75cm diameter placed at the end of tube causing the formation of a synthetic jet with velocities up to 10 m/s.

James *et al* [3] studied formation of a synthetic jet, produced normal to and at the center of a submerged oscillating diaphragm in water. The cavitation bubbles formed on the surface of the diaphragm and deflated during each cycle while travelling downstream. Comparison between the synthetic jet and a conventional turbulent jet in water showed a similarity of the time-averaged jet structure. Jet width growth and inverse centerline velocity are both linear functions of the distance from the actuator.

Development of a synthetic jet was studied experimentally by Smith and Glezer [7]. Measurements were taken in air through a rectangular orifice with 0.5 mm width and 75 mm length. According to their study synthetic jet is made by the time-harmonic formation and interaction of a train of vortex pairs that are produced at the edge of the orifice. A piezoelectric driver with 1140 Hz nominal resonance was used to vibrate a round diaphragm which was mounted in a sealed cavity.

As the diaphragm moves towards the orifice (chamber becoming smaller) flow is ejected through the orifice. This flow separates at the edge of the orifice and forms a vortex field which later rolls into a vortex pair traveling downstream due to its momentum. The exit radius of the orifice can change the rate of flow separation from the edges. As the diaphragm moves away from the orifice; suction occurs and if the rolled vortex pair has moved far enough from the orifice, it is not drawn back flow into the chamber of the actuator. However, surrounding fluid is drawn into the chamber resulting in a Zero-Net-Mass-Flux out of the orifice. Elements of fluid are exchanged between the chamber and outer media and the net hydrodynamic impulse of the vortex pairs is not zero. Smith and Glezer [7] also introduced two dimensionless parameters for synthetic jets: Stroke Length and Reynolds number. The vortex pair formation is governed by Stroke Length. In fact a study of vortex formation gives parameters ranges required for formation. A brief description of synthetic jet parameterization is given in Chapter 1 of this thesis.

Smith and Glezer [8] in another study, divided synthetic jet formation into two fields: near field formation and far field formation. Near the jet exit plane the flow is subjected to a time-periodic formation and downstream movement of vortex pairs which gradually become turbulent and interacting eventually creating a fully developed turbulent jet. Similarities between the later field and conventional 2-D turbulent jet were observed in their study far from the jet exit. They also found a stream wise decrease in synthetic jet’s momentum flux as a result of an adverse stream wise pressure gradient near the jet orifice, while for a conventional 2-D turbulent jet; the momentum flux is an invariant of the motion.

Synthetic jets have been compared with low Reynolds number continuous jets and also pulsed jets by Bera *et al* [24]. It is found that synthetic jets are produced by advection and interaction of vortices almost like a pulsed jet but they are formed by the working fluid of the flow system and thus transfer linear momentum to the flow system without net mass injection across the system boundary.

The early research of Smith and Swift [25] showed a resemblance in characteristic of low Reynolds number synthetic jets and high Reynolds number continuous jets. Later, they compared synthetic jets and continuous jets and explored the effect of dimensionless parameters on synthetic jets [1]. It was discovered that although synthetic jets and continuous jets have the same profile, synthetic jets grow more rapidly in terms of jet width and volume flux. Their research is the motivation of this work. A rectangular slot with cross-stream width of 75 mm was chosen for the experiment. Measurements were performed in air using a single hot-wire. Oscillations were generated using a set of eight loudspeakers in the frequency range of 10 to 100 Hz. Velocity amplitudes of up to 50 m/s were achieved at the exit plane. U_o was used to define Reynolds number for synthetic jets ($\mathrm{Re} = \frac{U_o h}{\nu}$) and U_{ave} was applied as a velocity scale for continuous jets ($\mathrm{Re}_h = \frac{U_{ave} h}{\nu}$). Schlieren images of the synthetic jets showed that cross-stream growth of the jet begins much closer to the exit plane for a synthetic jet than for a continuous jet [1].

There are many factors involved in studying synthetic jet behavior. Of those, the exit geometry of the orifice is of interest in many studies. Fugal [26] focused on how the exit geometry and non-dimensional Stroke Length could affect the formation threshold of the synthetic jet. The net momentum flux in the jet and the location of the stagnation point during half of the cycle (suction phase) was determined in their experiment [27]. In the first ejection phase of the flow, since all the fluid is moving away from the exit plane, there is no stagnation point. A stagnation point is formed during the suction phase of the cycle downstream from the exit plane. The flow entering from the sides to the channel is separated from the flow travelling away from the exit plane at this point; hence, the fluid downstream from the stagnation point continues to move away from the exit, while the fluid below the stagnation point moves into the channel. The downstream location of the stagnation point determines the size of the stream tube that contains the flow entering the channel [27].

Crook and Wood [28] also studied the effect of cavity and orifice geometry on synthetic jet formation. In order to facilitate changing the cavity height and orifice diameter, they constructed a shaker driven modular set up where different circular orifice plates can be interchanged. Smoke particles were used for visualization. The oscillator was set at 50.1 Hz. Reynolds number was computed with the hot-wire anemometry measurement of maximum centerline velocity during the ejection phase of the cycle. A vortex ring is formed when maximum value of circulation is reached. The excess circulation flow or vorticity that could not reach the maximum value will shape a tail behind the ring. The "tail" forms due to insufficient Reynolds number which causes the vortex ring not to roll up. Smith *et al* [29] also observed the tail behind a ring in their experiment. Figure 3 [4] shows the two dimensional images of the smoke seeded flow field as a function of Reynolds number and height to diameter aspect ratio. The white vertical line shows the approximate location of the orifice the white horizontal bars represent the approximate diameter of the orifice. The "tail" is shown in the figure with white arrows. The Reynolds number decreases from top to bottom and increases from left to right.

Two sets of measurements were taken in Smith *et al* [29]. In the first set they increased the orifice height while holding Reynolds number and orifice diameter constant. The second set was taken by increasing the height of the cavity while holding Reynolds number, orifice height and orifice diameter constant. In both experiments the amount of circulation in the ring increased due to generating a more developed velocity profile in the orifice. It was also found that a larger cavity would allow the ring to generate more vortices while interacting with the cavity wall.

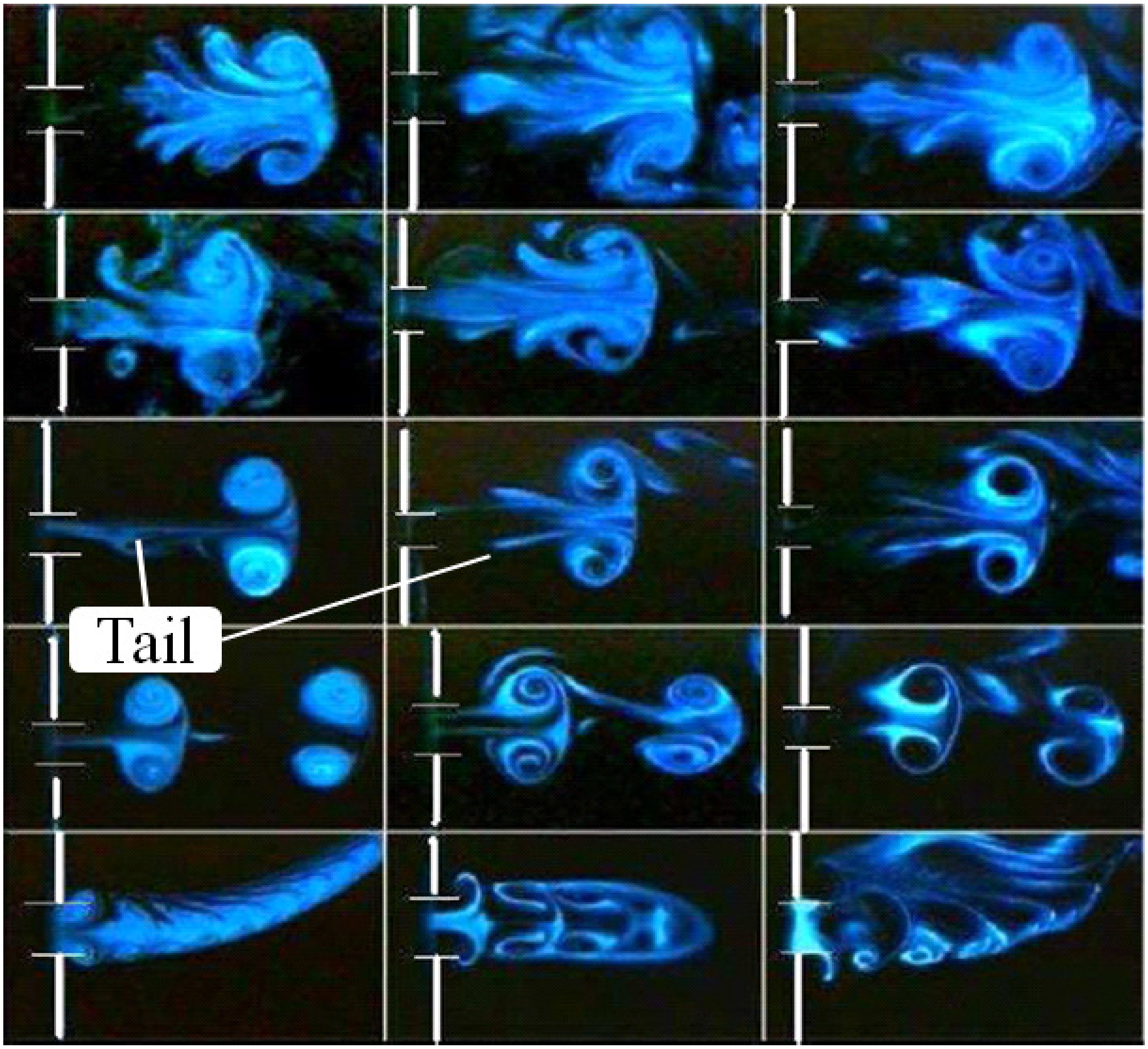

Figure 3 Effect of Reynolds number and orifice height-to-diameter aspect ratio on synthetic jet formation. Adopted from Holman [4].

Chen et al [12] used stroboscopic flow visualization to observe the occurrences of a laminar synthetic jet at low Reynolds numbers and turbulent synthetic jet at high Reynolds numbers using hot-wire anemometry to measure the velocity field. They were the first researchers to develop a piezoelectric actuator with a rectangular (35.5× 0.5 mm) orifice to produce synthetic jets. They recognized the presence of discrete vortex fields downstream of the orifice at low Reynolds number, however only one vortex pair was observed at the orifice at high Reynolds number, followed by a turbulent jet. They found both that the transition to turbulent flow depended on Reynolds number and dimensionless Stroke Length.

Particle Image Velocimetry (PIV) was used in some studies of synthetic jets. Bera *et al* [24] used PIV to measure velocity fields of a 100×1 mm^2 rectangular orifice. They used acoustic drivers (speakers) driven at a frequency of 200 Hz and found that the ejected fluid moved far downstream from the orifice during the ejection phase and was not affected by the suction phase. Stagnation point length was observed to be at distance of approximately two slot depths downstream of the orifice. Any particle above this point could not be affected by the suction phase of the flow. Above this point the flow was similar to a conventional steady jet.

Cater and Soria [30] also used PIV in their experiment. A round synthetic jet with a 2 mm diameter orifice was placed in a water tank and was driven by a piston cylinder arrangement that could oscillate with a time-periodic function to generate a sine wave. Their study demonstrates similar cross-stream distribution of velocity to conventional continuous jets but with a larger spreading rate. Using dye visualization in their study, they observed four distinct flow patterns as the Reynolds number increased. Figure 4 shows these patterns. The experiment was conducted beginning with low Reynolds number and gradually increasing. The first pattern as shown in Figure 4 (a) was a laminar- like flow which did not mix with the surrounding fluid and was referred to as “laminar jet” in their study. Figure 4 (b) revealed an individual laminar vortex ring that ended up combining and forming a transitional-like flow shown in Figure 4(c) which is then followed by a fully turbulent jet at the highest Reynolds number, shown in Figure 4(d). This pattern was called a “turbulent jet” which is very similar in appearance to a conventional continuous turbulent jet.

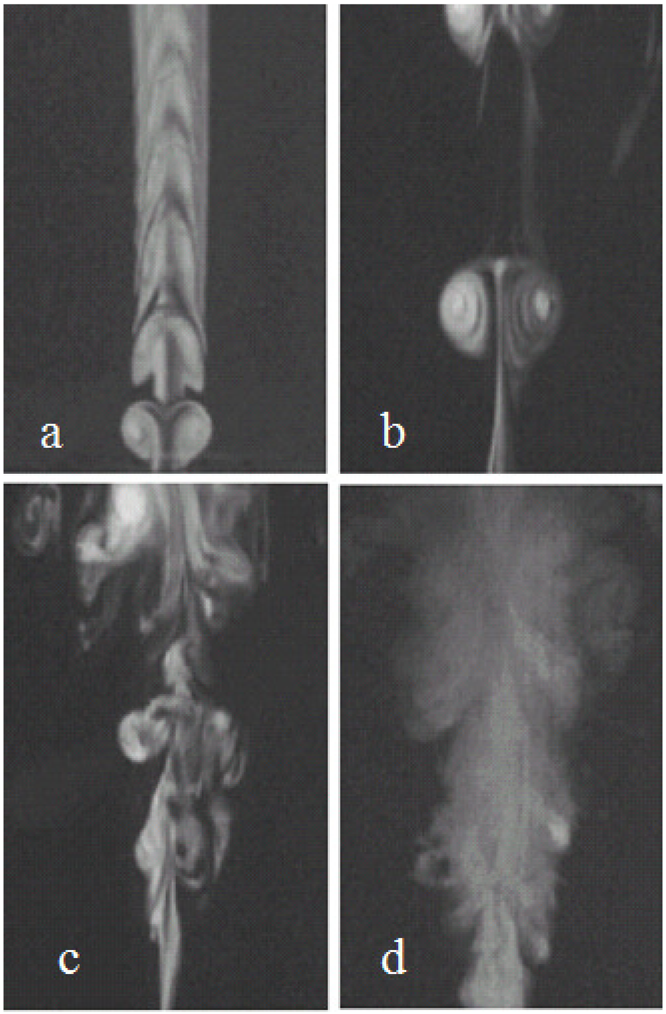

Figure 4 Flow regions as a function of Reynolds number: (a) laminar jet, (b) laminar rings, (c) transitional jet, (d) turbulent jet [30].

Zaman and Milanovic [31, 32] also did an experimental investigation on round synthetic jets with different geometries. They worked on high Reynolds number jets up to 46,000 with a fully turbulent flow in the absence and presence of a cross-flow. For synthetic jet formation, the threshold is found to be $L_o/d \simeq 0.5$ in absence of the cross-flow. In the presence of the cross flow, the penetration length of synthetic jet is found to depend on momentum flux ratio. Mean velocity, stream wise vorticity and turbulent intensity profiles of synthetic jets were observed to be similar to those of steady jets in cross-flow. They continued their study by exploring different geometries such as cylindrical, pitched and clustered while keeping the cross-sectional area constant. Figure 5 shows different geometries used in their study.

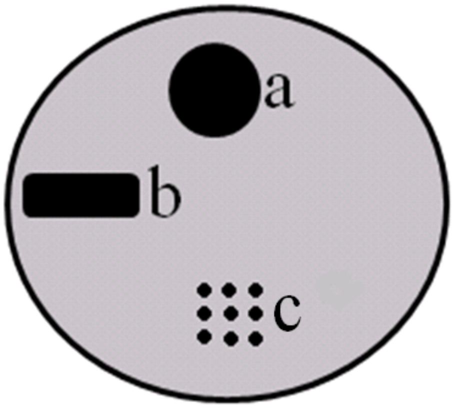

Figure 5 Different geometries: a) cylindrical, b) pitched and c) clustered.

In recent years, designing [33] and optimizing [5] the actuators has been studied. Straight, beveled and rounded plates were used for orifices in Shuster and Smith [6]. By using different designs of the orifice plates, velocity fields could be changed. In their study they used three different designs to investigate the effects of each on the formation of synthetic jets. Figure 6 shows the different orifice cross-sections used in their study. The height to diameter aspect ratio was held constant at 0.5. A piston cylinder was used to generate synthetic jets in water. PIV measurements showed the transition from laminar flow to turbulent flow is a function of Reynolds number and Stroke Length. Different geometries can result in different characteristic of vortex rings. The vortex rings formed through the beveled orifice persisted longer than the other two.

Mallinson *et al* [34] conducted an experimental-computational study on an axisymmetric orifice, oscillated by a piezoelectric driver. The oscillation frequency, orifice diameter and cavity height were changed. Hot-wire centerline velocity measurements showed that a larger cavity size had the effect of decreasing the jet velocity.

Smith *et al* [29] showed that the sharpness of the orifice slot could affect the jet formation. The jet formed at lower Reynolds number if the sharpness of the cavity increased.

Holman *et al* [35] also tried to find a relation between radius of curvature of the orifice exit edges and jet formation. They proposed a modified jet formation criterion which was related to the distance of formed vortex rings separating from each other.

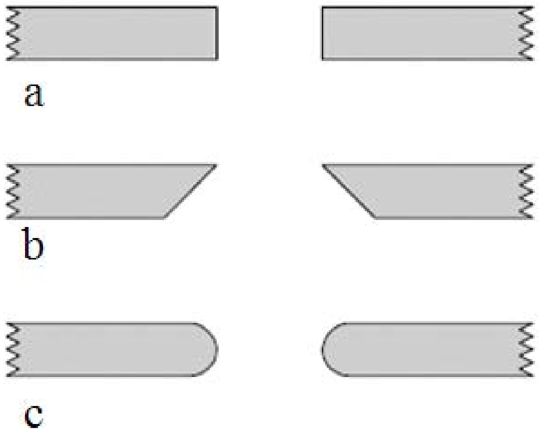

Figure 6 Orifice plate cross-sections used by Shuster and Smith: (a) straight, (b) beveled, (c) rounded [6].

2.3 Objectives

This experimental study is intended to provide velocity fields for a round synthetic jet at low velocities. The relationships between the flow velocity and parameters such as diameter of the orifice and frequency are explored. The detailed objectives of this study are:

1. To investigate the variations of the dimensionless time mean velocity across the exit plane of the synthetic jet.

2. To investigate the variations of dimensionless time mean velocity along the centerline in the near field and far field regions.

3. To investigate the variations of the dimensionless velocity in the radial direction at various axial distances downstream of the orifice exit.

Chapter 3

EXPERIMENTAL METHODOLOGY

This chapter provides a description of the synthetic jet actuator device used in this experimental study. Details of the experimental apparatus, data acquisition procedure and data processing techniques used for the analysis are provided.

3.1 Experiment Apparatus

The experiment apparatus consists of six major categories (synthetic jet device, signal generating equipment, traverse equipment, calibration system, velocimetry equipment (hot-wire anemometer) and computer software). Components of each category will be explained in this section. A block diagram of the setup is shown in Figure 7 and the experimental apparatus is shown in Figure 8 and Figure 9.

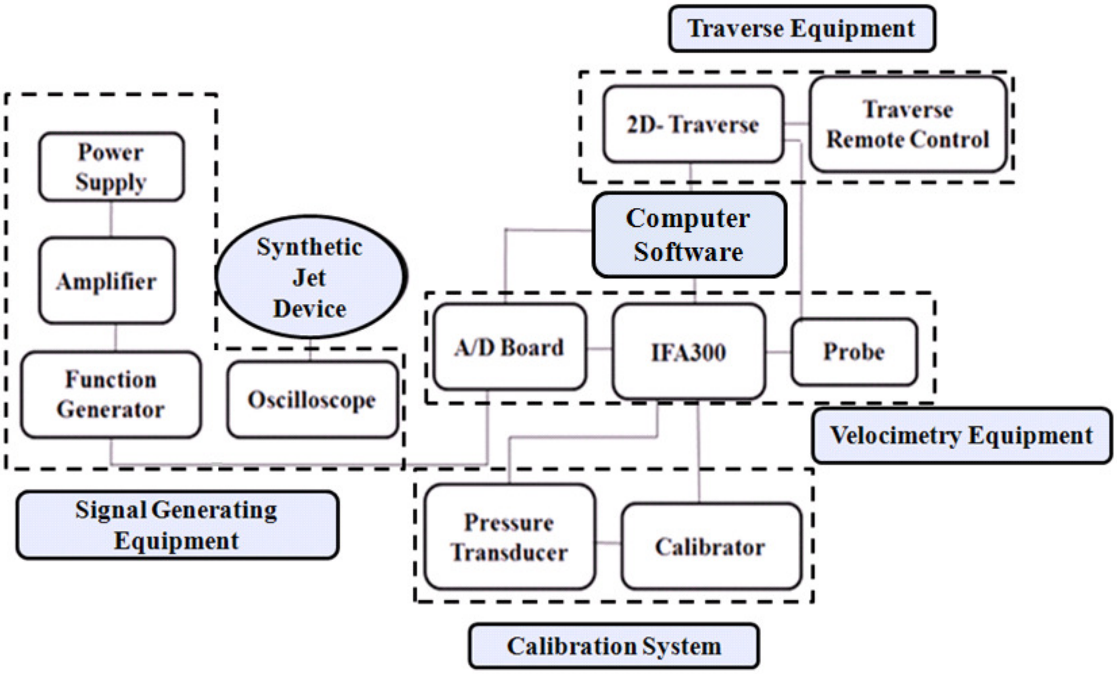

Figure 7 Block diagram of experiment setup.

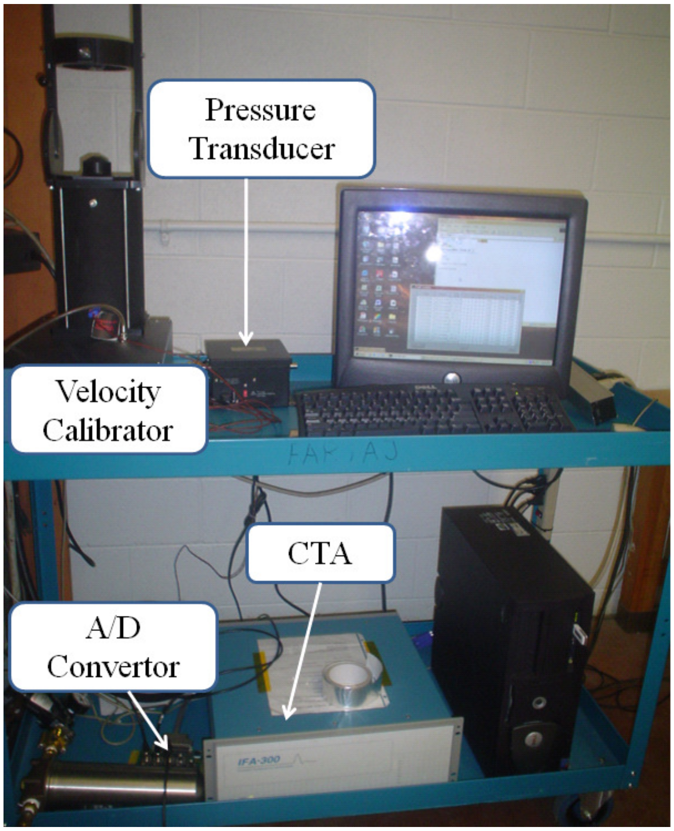

Figure 8 Hot-wire Anemometry, calibrator and computer.

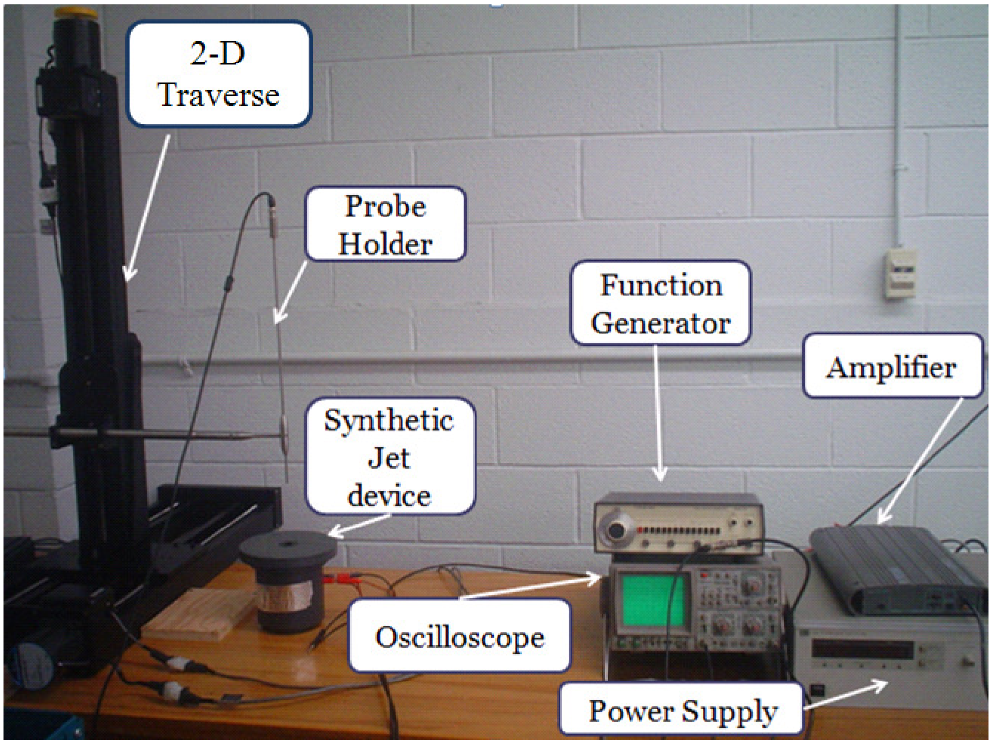

Figure 9 Synthetic jet device, signal generating and traverse equipment.

3.1.1 Synthetic Jet Device

The synthetic jet device driver is a Logitech computer loudspeaker nominally rated at 32 Watt power. The speaker is considered as an acoustic driver. Schematic details and dimensional parameters are shown in Table 1 and Figure 10. Since one of the parameters is the orifice diameter, the speaker lid is designed to have a snap on changeable orifice plate to allow two different orifice diameters. Orifice diameters of 10 mm and 15 mm are used in this experiment. The outer edge of the orifice has a 0.5 mm radius in order to prevent flow separation (Figure 10). The synthetic jet device is fixed to the experiment table to prevent vibration and dislocation errors.

Orifice diameter d (mm)	Orifice slot height h (mm)	Radius curvature R (mm)	Cavity Volume V (m^3)
10 and 15	4.36	0.5	259.5×10^{-6}

Table 1 Synthetic jet device specification parameters.

3.1.2 Signal Generating Equipment

The signal generating equipment includes a function generator (Wavetek Model 182A) to generate the input signal for the oscillator (speaker driver). The signal type is chosen to be sinusoidal with an 8 volt peak to peak amplitude. Signal frequency is one of the parameters that is changed in this research. Measurements were taken with frequencies of 10 and 20 Hz. The function generator output signal is connected to an amplifier (MEI two channel bridgeable design - multi mode power DA8500) via a 50 Ω out low resistance BNC connection port. A DC power supply (HP Model 6011A) is used to provide 14 volts for the amplifier. An oscilloscope is connected to speaker input to measure signal amplitude and observe the signal shape. The chamber of the speaker is completely sealed to maintain a more uniform air flow in the cavity.

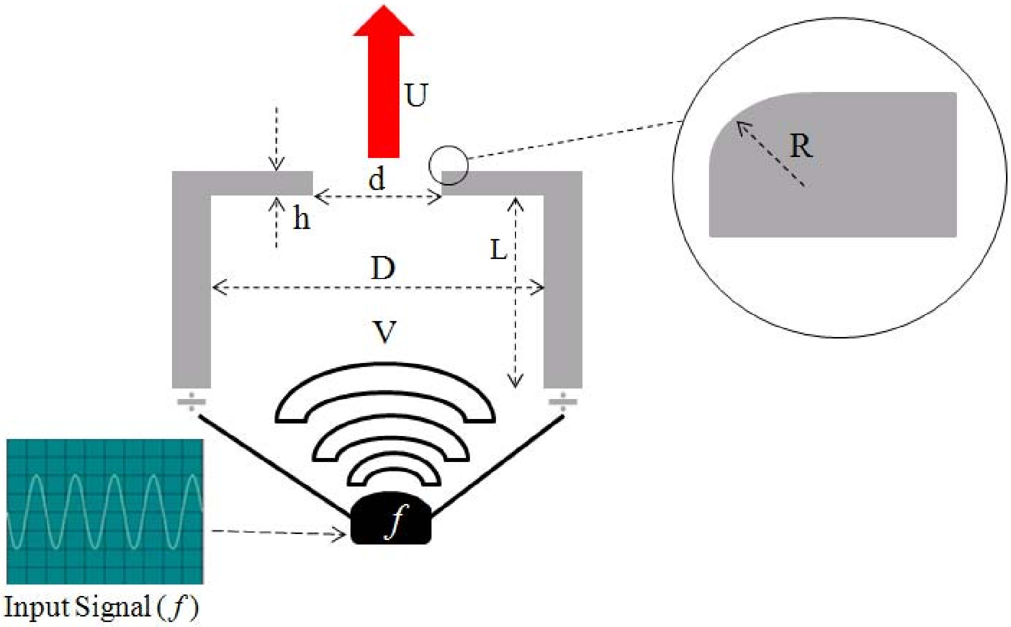

Figure 10 Detailed schematic of synthetic jet dimensional parameters.

3.1.3 Traverse Equipment

A Velmex VXM stepper motor controller is used to traverse the probe into different locations. A two-dimensional traverse is used to accommodate specific positions for the experiment measurements. The probe can be moved in the X and Y direction (Type M092- FD-447) with traversing speed of 2.5 mm/s. The motion can be controlled either with the remote controller or manually (Figure 11). A dial gauge is used to measure each step size estimating 200 steps in 1 mm. Resolution is calculated to be 0.005mm.

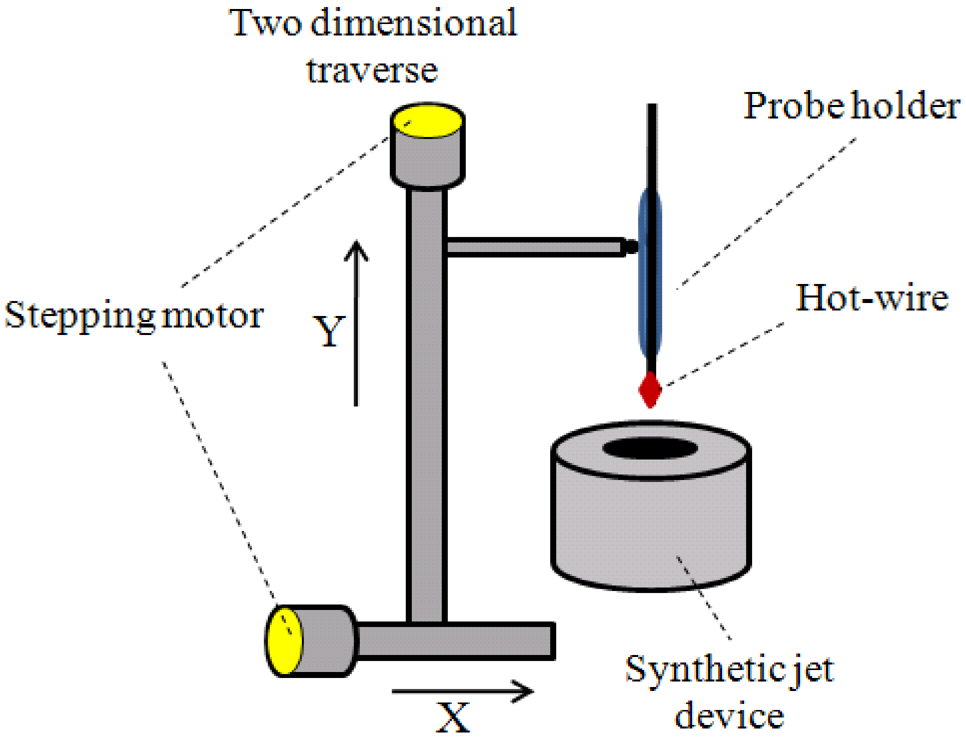

Figure 11 A schematic of the traverse location, hot-wire and synthetic jet device.

3.1.4 Hot-wire Anemometry

A single straight hot-wire anemometer system (TSI brand, IFA 300) with a Constant Temperature Anemometer (CTA) operating bridge is used in obtaining velocity measurements. It was selected due to the high frequency response, fine spatial resolution and wide velocity range. A CTA utilizes a wire or, in this study, a film which is heated to a temperature above the ambient by an electrical current. This film is located in one arm of a four-arm Wheatstone bridge. A servo amplifier is usually used to balance the circuit by controlling the current which is imposed on the film to keep the resistance and hence temperature constant. The voltage output from the CTA is proportional to the current required to be passed through the film to balance the Wheatstone bridge circuit. Operation of the hot-wire is based on the forced convective heat transfer rate from the probe to the fluid. The forced convective heat transfer rate depends on the velocity changes of the fluid. In other words, velocity changes cause the heat transfer coefficients to change and hence results in a change in temperature. The control system then, adjusts the amount of current passing through the hot-wire to maintain the hot-wire temperature constant.

There are five discrete elements in a hot-wire anemometer system: probe, probe holder, calibration system, analog to digital (A/D) converter and data analysis software.

Probe

A film probe is used for this experiment. They are more rugged and tend to retain their calibration better than wires. Table 2 shows the specification of the probe used for this experiment.

Sensor No.	Probe Type	Recommended Application Environment	Probe RES at 0°C (Ω)	Recommended Operation RES (Ω)	Recommended Operation Temperature (˚C)
51-51 TSI Model 1201-20	Film	Gas	6.19	9.49	250

Table 2 Specification of the probe, adopted from TSI, IFA300 probe box.

Probe Holder

The probe is attached to the probe holder and the probe holder is connected via a 5 meter standard cable to the IFA300 system.

Calibration System

Calibration provides a relation between output voltage and effective velocity in the form of an equation using King’s law or fourth order or higher order polynomial (in this study a 5^{th} order polynomial is chosen for the calibration curve fit). Figure 12 shows the calibration curve obtained in this experiment. The velocity range is set to be from 0 m/s to 5 m/s. An automated air velocity calibrator (TSI Model No. 1129) is used and “Thermal Pro Software” provides the calibration curve. Details of calibration procedure are explained briefly in Appendix B.

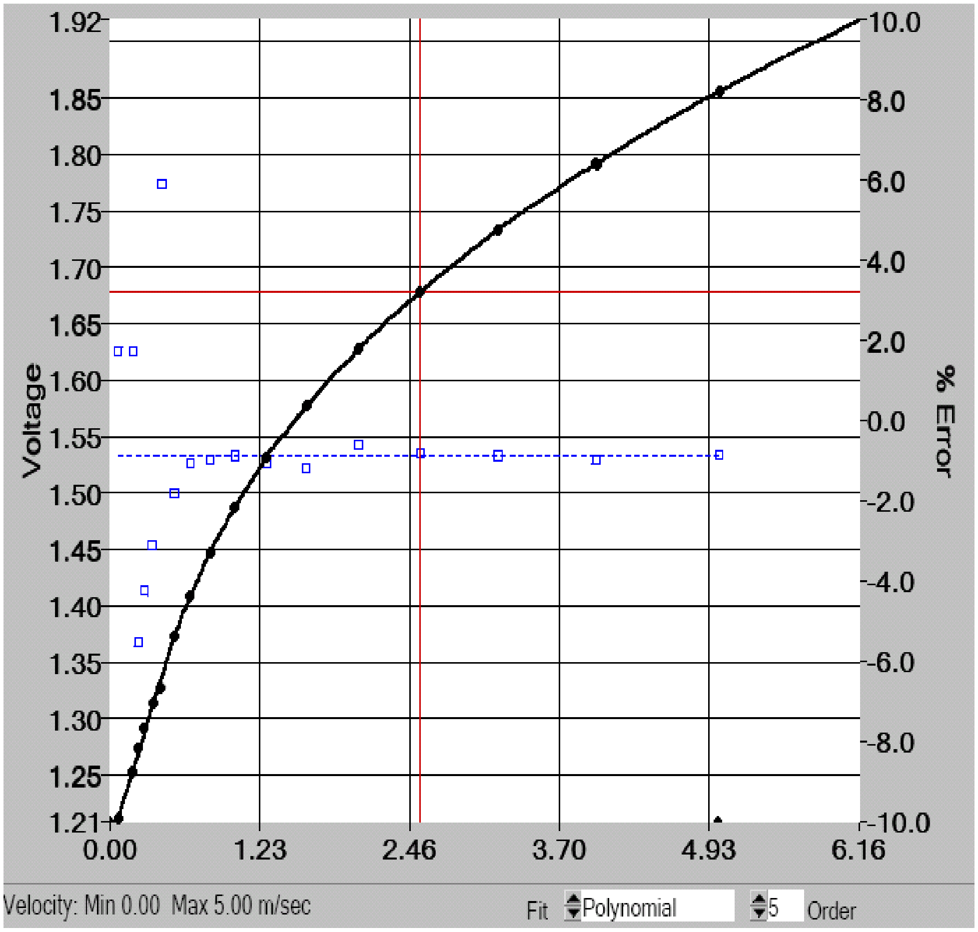

Figure 12 Calibration curve fitted by a polynomial 5th order curve.

The automated air calibrator consists of a settling chamber with a primary jet nozzle. The jet nozzle diameter can be changed depend on the expected velocity range to be measured. In this case a 14 mm primary nozzle is used. A secondary nozzle is also located in line with the primary nozzle in order to improve the accuracy and sensitivity at low velocity. A pressure transducer is also used to measure the pressure upstream of the free jet, or upstream of the nozzle. The transducer is a MKS Baratron type transducer with an output of 0 to 10 Volts DC for differential pressures of 0 to 100 mm Hg. Figure 13 shows the locations of the secondary and primary nozzles and details of the calibrator including pressure transducer, thermocouple, A/D converter board and also connections made between the components and computer. In all the experiments the room temperature was considered to be 20 ° C.

Analog to Digital Converter

A 12- bit A/D converter accepts voltage inputs in the range of –5 volts to +5 volts with a built in signal conditioner in the IFA 300 (TSI A/D board Type REV A). Up to a 5 volt offset and a gain of 1 to 10 are provided by the signal conditioner depending on the pressure transducer and anemometer output signal levels. The system is connected to the probe holder via a 5 meter cable with measured resistance of 0.36 Ω. Figure 14 shows the connections between A/D converter board and other components.

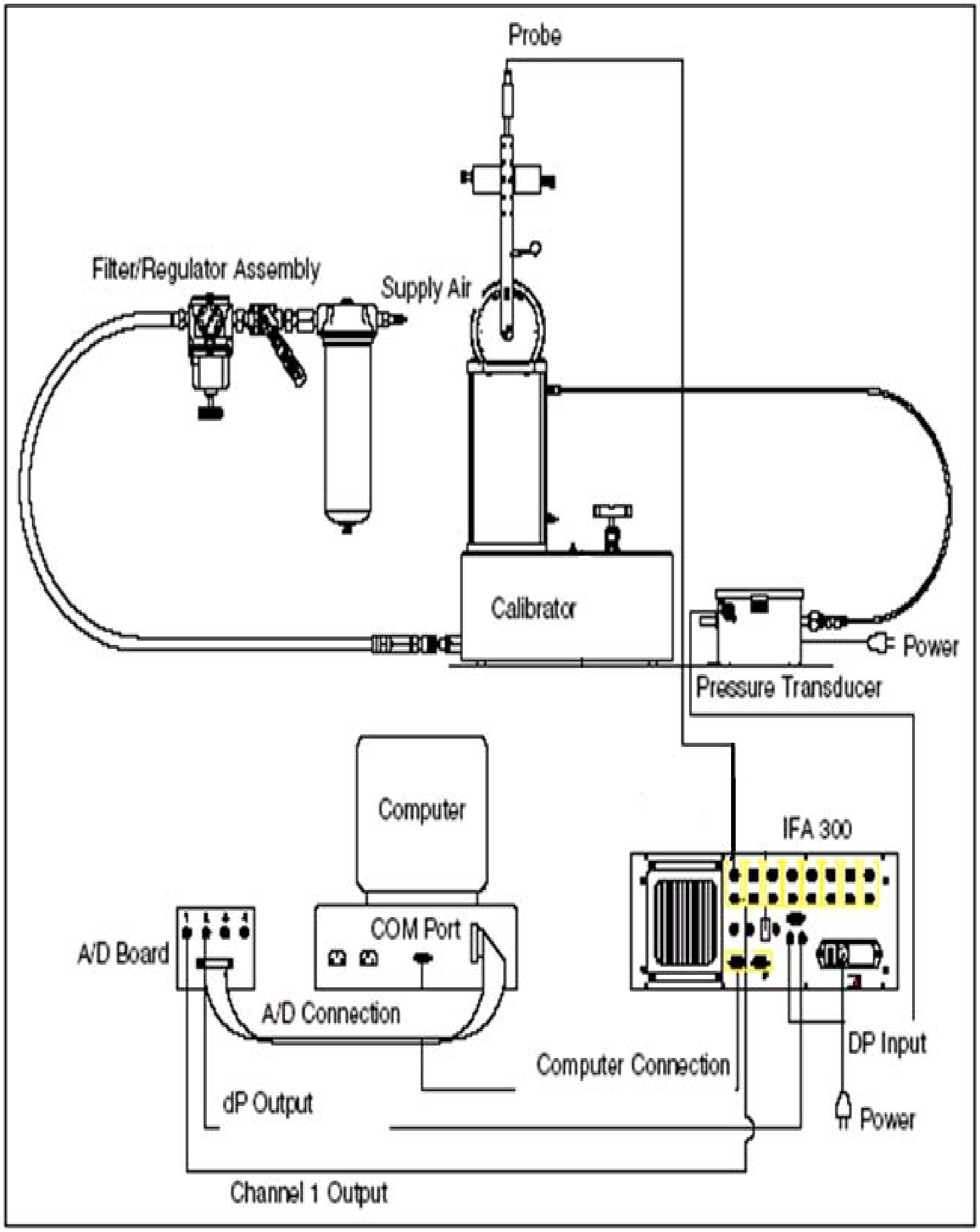

Figure 13 Connection between IFA300, air calibrator, pressure transducer, A/D board and computer [36].

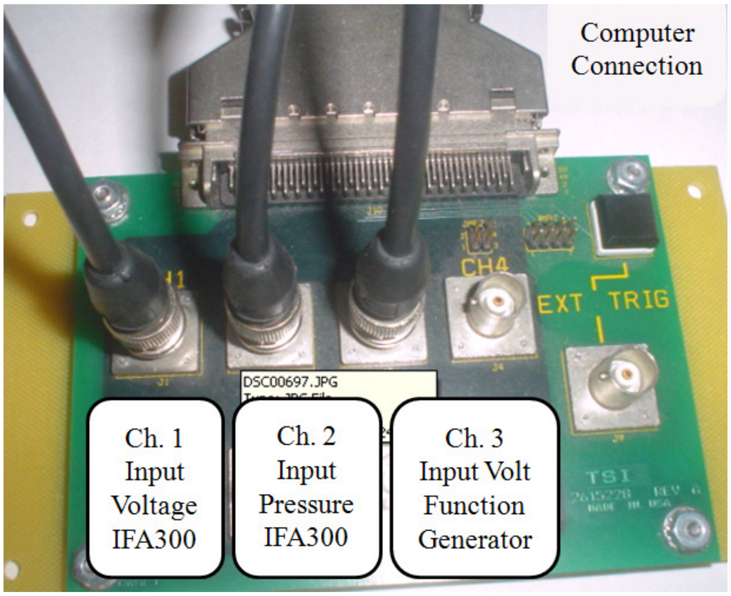

Figure 14 A/D board connections with function generator and IFA300.

Data Analysis Software

A PC computer is used for collecting and post-processing the data using “Thermal Pro Software”. The software is used to configure the IFA300 and for data acquisition and analysis. The software also assists in controlling the traverse, setting gain, offset and resistance. The automated air velocity calibrator is also fully controlled by the Thermal Pro software. It is used to determine the calibration points, set the calibration velocity range and fit the calibration curve.

Directional Ambiguity

Hot-wire Anemometry has limitations. The most serious limitation is directional ambiguity which means that hot-wire is insensitive to the flow direction.

The input signal from a hot-wire subjected to a sinusoidal change of the velocity over the hot-wire are shown in Figure 15. Instead of having two half cycles of negative and positive sign, it has two half cycles of positive sign. A synthetic jet has an ejection phase and a suction phase, the positive part of the cycle represents the ejection phase and the negative part represents the suction phase. In this thesis a method of overcoming this problem is used and a detailed explanation is given in Section 3.5.

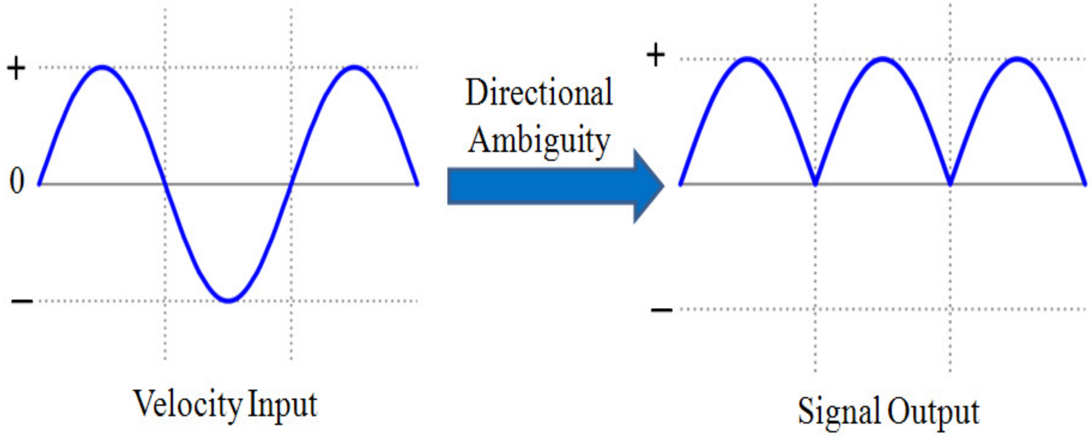

Figure 15 Effect of directional ambiguity on the output signal.

3.2 Experimental Procedure

In this study, velocity of the air flow in synthetic jets is measured. Measurements are made at various points in the flow field, for frequencies of both 10 and 20 Hz and orifice diameters of 10 and 15 mm. The experimental measurements are performed in air at atmospheric pressure.

At each position, 16 kilo points (16385 points) were taken with a 5000 point per second sampling rate which resulted in a total sampling time of 3.27 seconds. According to the sampling theorem, the sample rate must be greater than twice the highest of the maximum measured signal frequency $(f_s > 2f_{max})$ which is satisfied, in this experiment. Depending on the speaker excitation frequency, the synthetic jet period, changes. The synthetic jet period is defined as:

$$T = \frac{1}{f} \tag{11}$$

where T is the period and f is frequency. For frequencies of 10 and 20 Hz, this gives periods of 0.099 and 0.049 seconds respectively.

A 16 kilo point sample with 5000 point per second sampling rate is chosen after comparing the results with 4, 8 and 32 kilo point results. Figure 16 shows the U_{bar}/U_o values (which is the ratio of time-averaged velocity over downstream-directed velocity at X=0, see Section 1.2) versus the number of points. The higher number of points (32 kilo points) improves the results only by % 0.57. Taking 32 kilo points of data at each measurement would also need a faster and more appropriate processor for post-analyzing the data; hence 16 kilo points are taken instead of 32 kilo points.

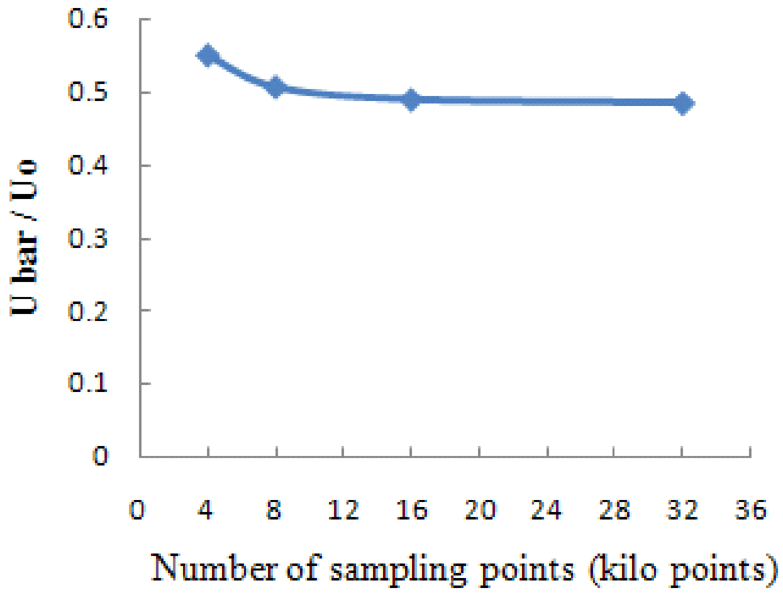

Figure 16 U_{bar}/U_o **versus number of sampling points.**

3.2.1 Data Acquisition

Using Thermal Pro software, probe resistance, temperature, sampling rate and number of points can be entered into the computer and then by clicking the ”Trigger” button, acquisition starts. Each set of data is measured after setting the position with the traverse control program. As mentioned before 16 kilo points are taken with 5000 points per second sample rate. Each cycle depends on the frequency consist of specific number of points at a fixed period for instance at 20 Hz frequency and the total time of 3.27 seconds, there are approximately 65 cycles measured and automatically saved to the computer ready to be extracted by the post-analysis option of the software. Appendix B offers more specific, step by step instructions for data acquisition using Thermal Pro software. There are three different categories of measurement points taken in this study:

1-Measurements at the orifice plane (X=0) which are taken at Center, North, South, West and East (Figure 17).

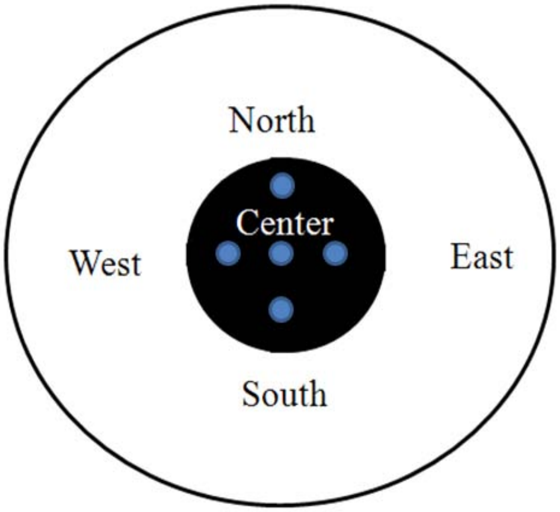

Figure 17 Measurement points at the orifice plate.

2- Measurements along the centerline of the orifice from X=0 to X=3d in d/4 intervals (Figure 18)

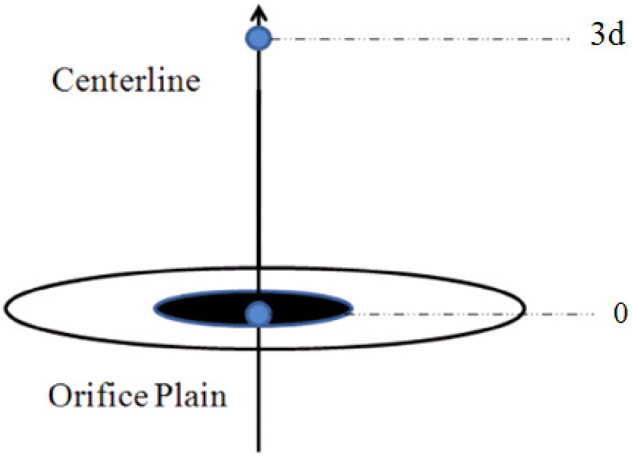

Figure 18 Measurement points along the centerline of the jet exit.

3- Measurements at various positions, perpendicular to the jet axis, moving from the center towards East and West at fixed axial distances from the jet exit. These measurements are taken in order to obtain the velocity profiles at axial distance at d/2 and 11d/4 (Figure 19).

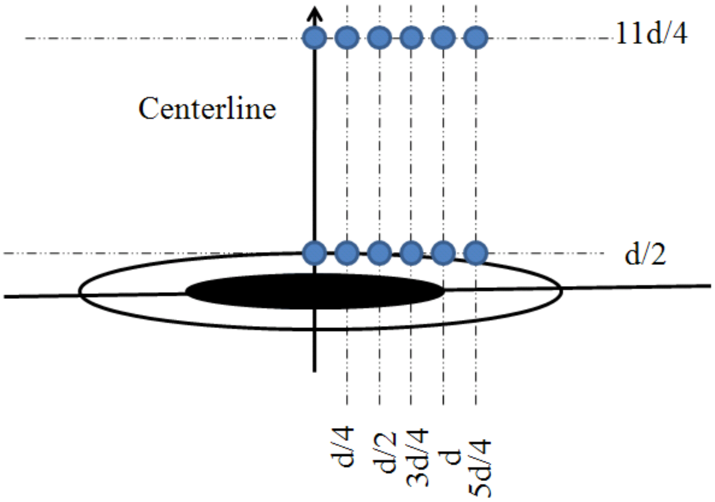

Figure 19 Measurement points at d/2 and 11d/4 axial distances, perpendicular to the jet axis.

3.3 Data Processing

Using the IFA300 post analysis software, data can be converted and extracted into a worksheet. Directional ambiguity makes it complicated to analyze the results. It is even harder as we traversed downstream along the centerline. Figure 20 shows the ejection and suction part of the cycle as the X/d increases. Traversing downstream away from the jet exit the ejection phase increases and suction decreases.

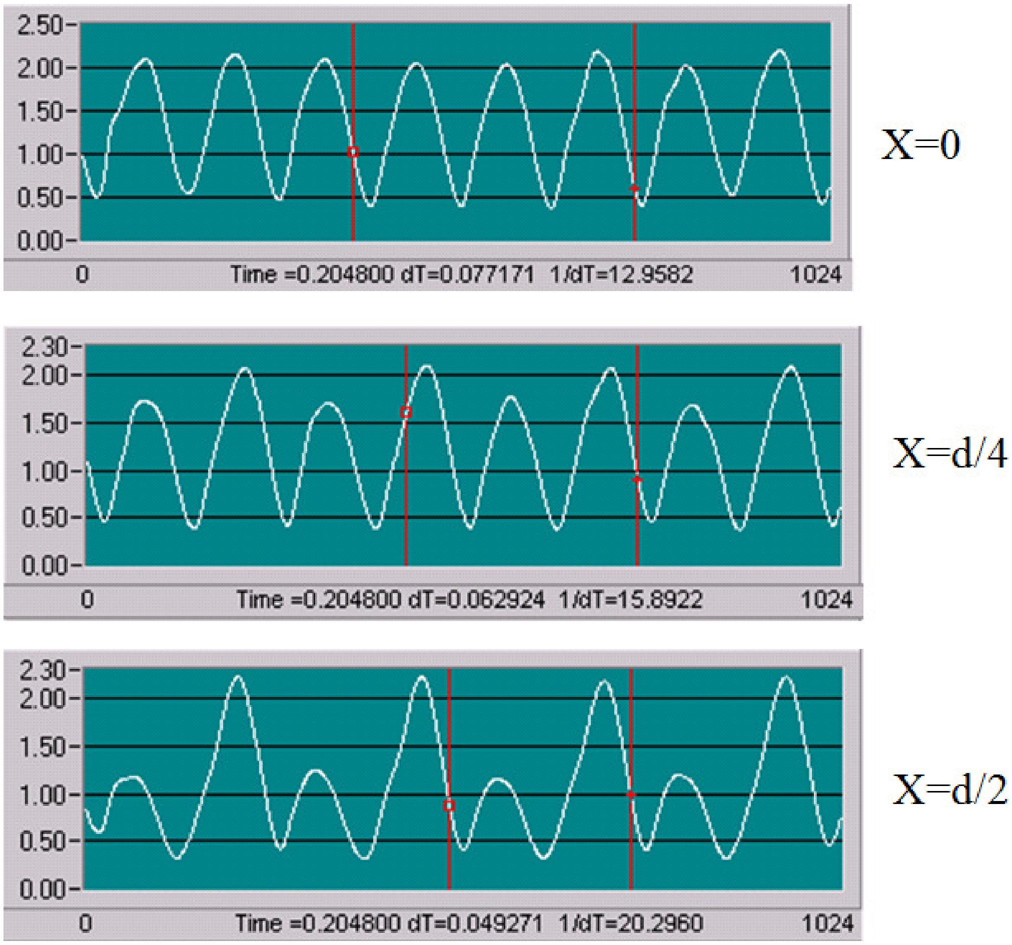

Figure 20 Ejection and suction phase along the centerline at X=0, X=d/2 and X=d/4.

To analyze the data sets, phase locked velocities are needed. This means each data cycle is extracted from the raw data and plotted over one cycle from t=0 to t=T. Excel is used to gather all the data points in one cycle. Figure 21 shows 33 measurement cycles layered in one cycle at X=0 at 10 Hz frequency for the 10 mm diameter orifice.

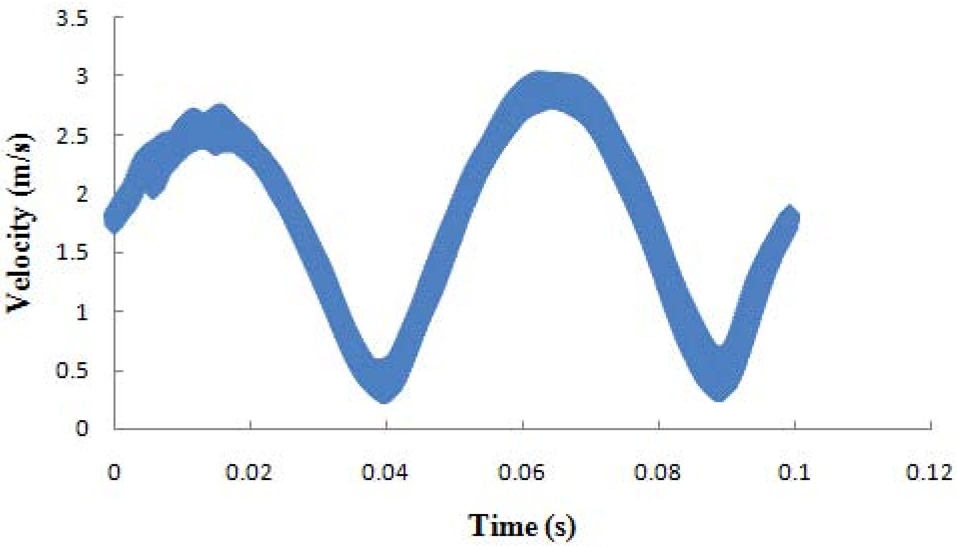

Figure 21 All 33 measurement cycles layered on one period for the 10 mm-10 Hz jet.

Fourier series is used to determine an average for the data points which retains the cyclic nature. Four terms of a Fourier series are used for curve fitting in this study (shown in Equation 12), since higher orders did not offer much more accuracy. A MATLAB curve fitting tool is used to find the coefficients ($A_0, A_1, B_1, \ldots$). A nonlinear least square curve fitting technique (Levenberg-Marquardt) is chosen as the fitting algorithm:

$$u_o(t) = A_0 + A_1 Sin(\omega t) + B_1 Cos(\omega t) \\ + A_2 Sin(2\omega t) + B_2 Cos(2\omega t) + A_3 Sin(3\omega t) \\ + B_3 Cos(3\omega t) + A_4 Sin(4\omega t) + B_4 Cos(4\omega t) \tag{12}$$

The resulting Fourier series can be plotted and represents all the layered cycles as shown in Figure 22. Since it is known that each cycle has a suction and an ejection phase and suction should be negative, cycle reversing can be done by finding the minimum points. Having the real ejection and suction phase, it is very straight forward that U_{bar} is the area under the curve of positive part of cycle minus area under the curve of negative part of cycle. The area can be determined by integration of the Fourier Series.

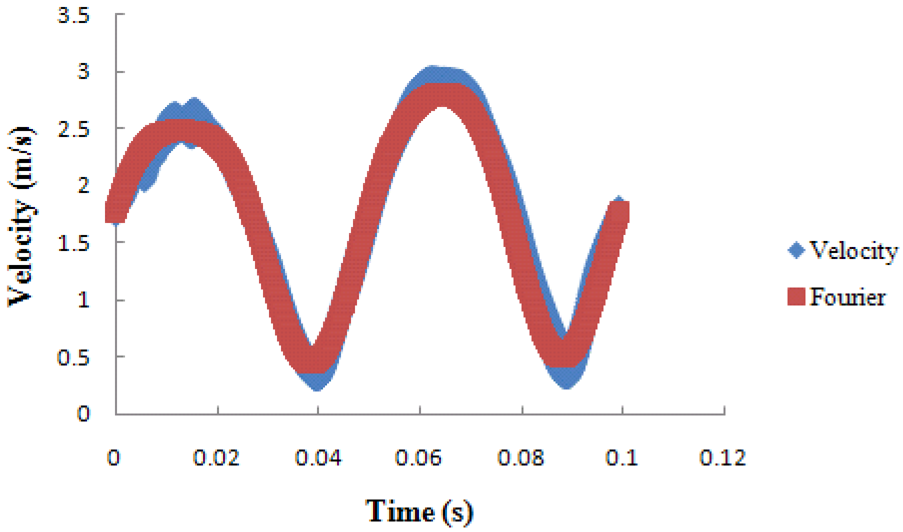

Figure 22 Fourier Series.

The Fourier Series, integrated over the whole period, is the value of U_{bar} which should theoretically be zero at center of the orifice plane, $U_{bar}$is given in Equation.13.

$$U_{bar} = \frac{1}{T}\int_0^T u_o(t)\,dt$$

$$= \frac{1}{T}\Big[A_0 t - \frac{A_1}{\omega}Cos(\omega t) + \frac{B_1}{\omega}Sin(\omega t)$$

$$- \frac{A_2}{2\omega}Cos(2\omega t)\frac{B_2}{2\omega}\ Sin(2\omega t)$$

$$- \frac{A_3}{3\omega}Cos(3\omega t) + \frac{B_3}{3\omega}\ Sin(3\omega t)$$

$$- \frac{A_4}{4\omega}Cos(4\omega t) + \frac{B_4}{4\omega}\ Sin(4\omega t)\Big]$$

(13)

The value of U_o can also be determined by integrating the Fourier Series over only half of the cycle shown in Equation 14. Figure 23 shows the cycle of the Fourier Series, corrected for directional ambiguity.

$$U_O = \frac{1}{T}\int_0^{\frac{T}{2}} u_o(t)dt$$

$$= \frac{1}{T}\Big[A_0 t - \frac{A_1}{\omega}Cos(\omega t) + \frac{B_1}{\omega}Sin(\omega t)$$

$$- \frac{A_2}{2\omega}Cos(2\omega t) \ + \frac{B_2}{2\omega}\ Sin(2\omega t)$$

$$- \frac{A_3}{3\omega}Cos(3\omega t) + \frac{B_3}{3\omega}\ Sin(3\omega t)$$

$$- \frac{A_4}{4\omega}Cos(4\omega t) + \frac{B_4}{4\omega}\ Sin(4\omega t)\Big]$$

(14)

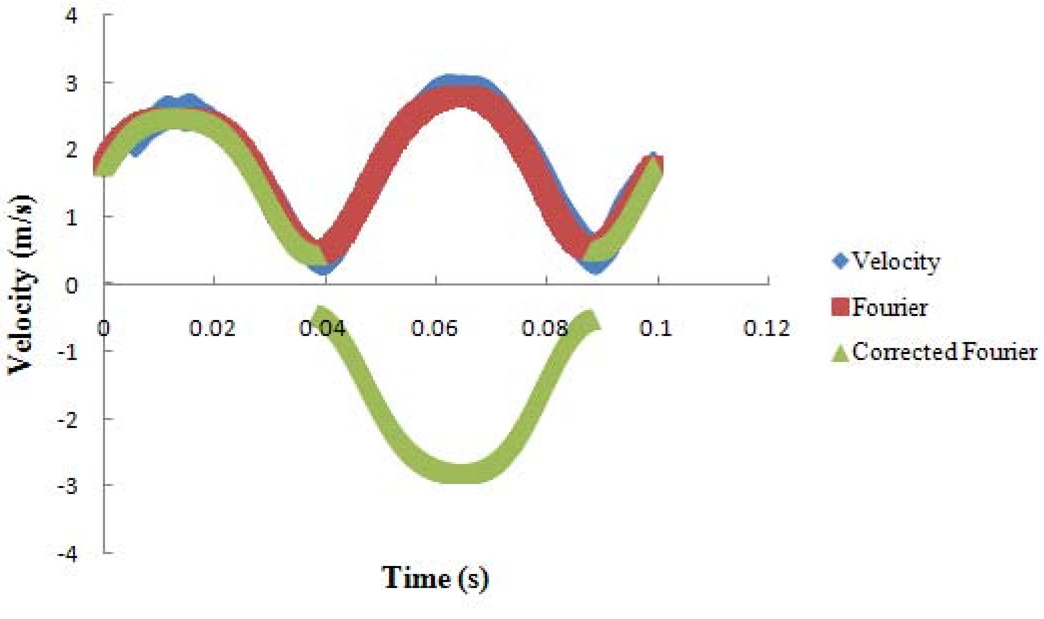

Figure 23 Reversing the suction cycle by using Fourier Series and the minimum point.

Chapter 4

RESULTS AND DISCUSSION

Results of measurements are presented in this chapter. All the data used to plot the figures can be found on an attached CD-ROM following the guidelines given in Appendix C. Section 4.1 includes a study on the orifice exit plane. Section 4.2 discusses the results of the centerline velocity measurements which are compared with Smith and Swift [1], Cater and Soria [30] and Smith and Glezer [7]. Section 4.3 offers the radial velocity profile results.

4.1 Orifice Exit Plane Study

The dimensionless average velocity, U_{bar}/U_o , for the five measured points in each set of data: Center, East, West, North and South on the orifice exit plane for the case of 10mm-10 Hz, 10 mm-20 Hz, 15 mm-10 Hz and 15 mm-20 Hz can be found in Table 3, Table 4, Table 5 and Table 6. Figure 24, Figure 25, Figure 26 and Figure 27 show the same results with error bars in a 3-D plot (bar scale format). One end of the bar, in each case, is located at $U_{bar}/U_o = 0$.

Position	Z	Y	U bar/U o
Center	0	0	0.063
East	2.5	0	0.114
West	-2.5	0	-0.050
South	0	-2.5	-0.076
North	0	2.5	0.074

Table 3 Probe positions on the orifice plane and U_{bar}/U_o values for 10 mm diameter at 10 Hz.

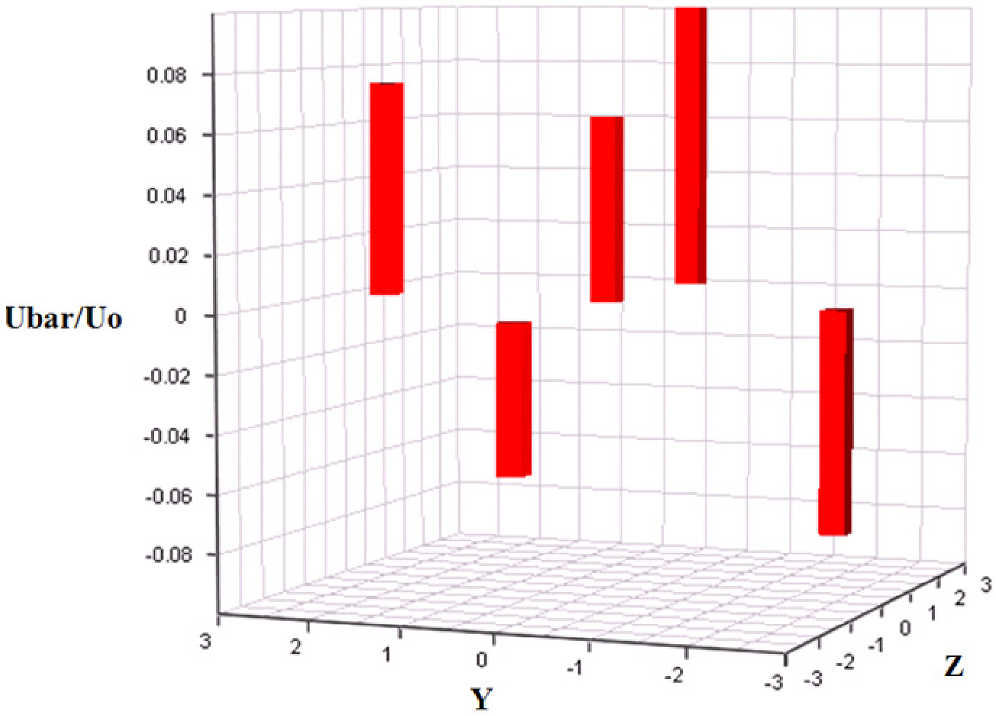

Figure 24 3D plot at the orifice plane for 10mm diameter and 10 Hz frequency.

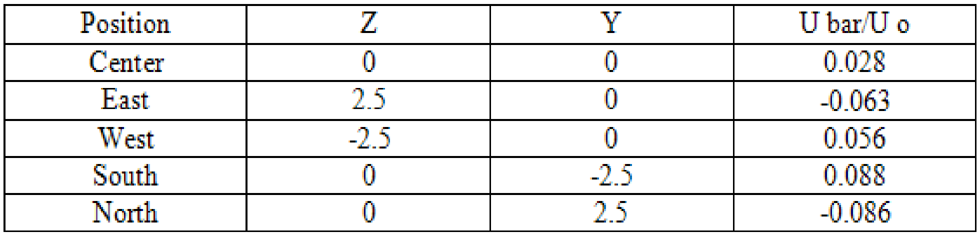

Position	Z	Y	U bar/U o
Center	0	0	0.028
East	2.5	0	-0.063
West	-2.5	0	0.056
South	0	-2.5	0.088
North	0	2.5	-0.086

Table 4 Probe positions on the orifice plane and U_{bar}/U_o values for 10 mm diameter at 20 Hz.

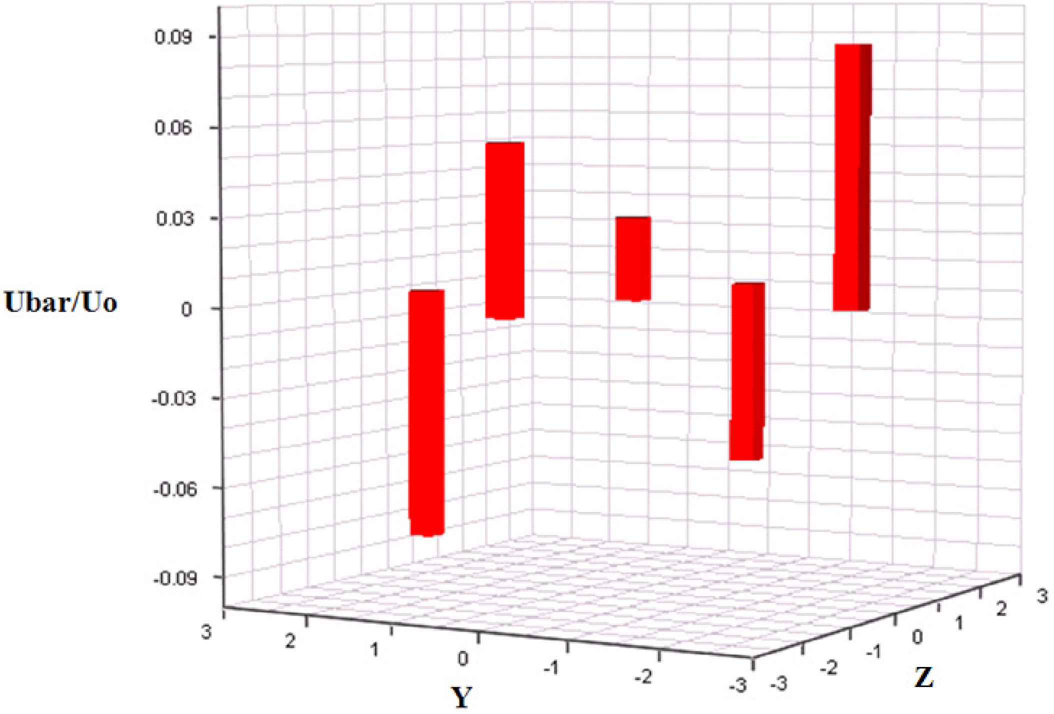

Figure 25 3D plot at the orifice plane for 10mm diameter and 20 Hz frequency.

Position	Z	Y	U bar/U o
Center	0	0	0.046
East	3.75	0	0.029
West	-3.75	0	0.029
South	0	-3.75	-0.078
North	0	3.75	-0.012

Table 5 Probe positions on the orifice plane and U_{bar}/U_ovalues for 15 mm diameter at 10 Hz.

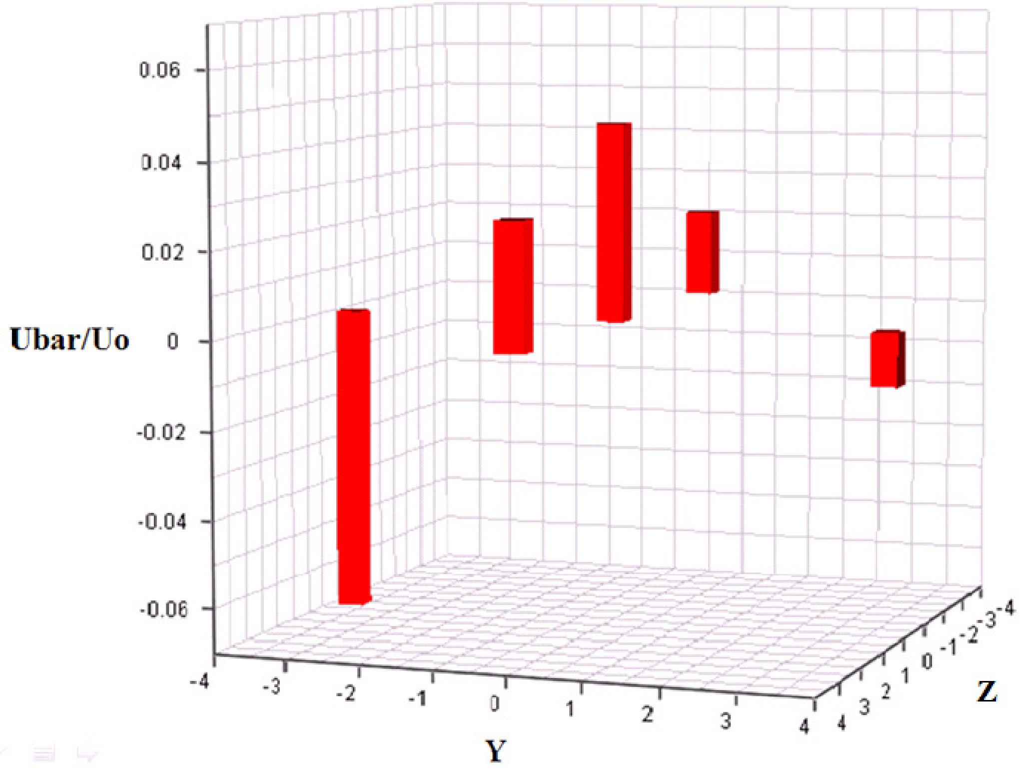

Figure 26 3D plot at the orifice plane for 15mm diameter and 10 Hz frequency.

Position	Z	Y	U bar/U o
Center	0	0	-0.039
East	3.75	0	-0.024
West	-3.75	0	0.061
South	0	-3.75	-0.087
North	0	3.75	-0.078

Table 6 Probe positions on the orifice plane and U_{bar}/U_ovalues for 15 mm diameter at 20 Hz.

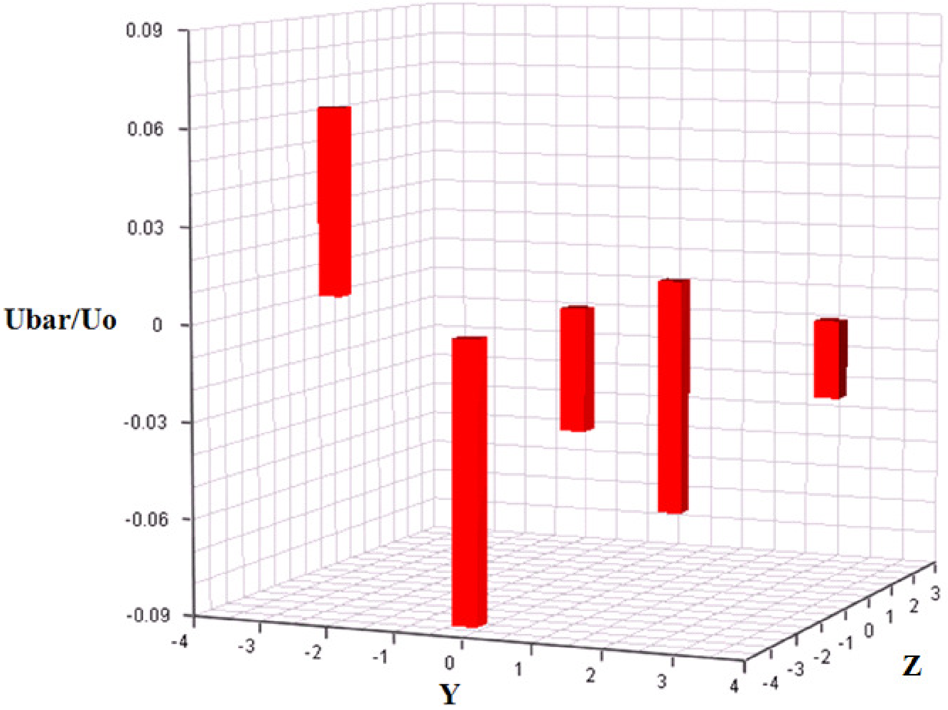

Figure 27 3D plot at the orifice plane for 15mm diameter and 20 Hz frequency.

Due to the Zero-Net-Mass-Flux characteristic of the device and its axially symmetric geometry, it might be expected that the U_{bar}/U_o values across the exit plane would be uniform and equal to zero. Although the results in each case show that the values are very small, they are not zero and vary slightly across the orifice plane.

It is seen that the velocities in the case of smaller orifice diameter, tend to have slightly larger magnitude. Table 7 shows U_0 values at the center of the orifice (Z=0, Y=0). As it is seen, 10 mm-20 Hz jet values are larger than the 10 mm-10 Hz jet. The results show the same trend for the 15 mm-10 Hz jet and 15 mm-20 Hz jet. Also the 10 mm-10 Hz jet values are larger than the 15 mm-10 Hz jet.

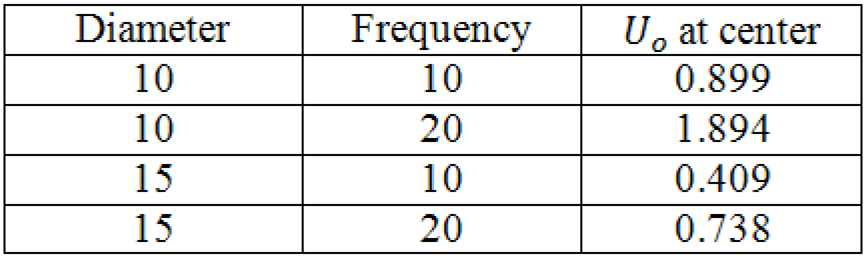

Diameter	Frequency	U_o at center
10	10	0.899
10	20	1.894
15	10	0.409
15	20	0.738

Table 7 U_o values at center of the orifice.

Although the orifice is axisymmetric, the results show that the velocity variation is not completely uniform over the orifice plane. This could be caused by a non-uniform oscillating driver due to aging, contamination or non-uniform sealant under the drivers cap. The device chamber is sealed with aluminum tape in order to ensure that there is no leakage of air; however a non-uniform leakage could be another reason for the non-uniform velocity. It is also observed that the pattern of variation is not consistent for each case. The negative values are not always at the same location. This might be due to standing wave pattern differences within the chamber.

4.2 Synthetic Jet Centerline Study

In order to compare the obtained results with the previous studies, the data values are plotted using U_{bar}/U_o versus X/d as shown in Figure 28.

Error bars for one of the cases are included showing a 3% uncertainty in U_{bar}/U_o values (see Section A.7)

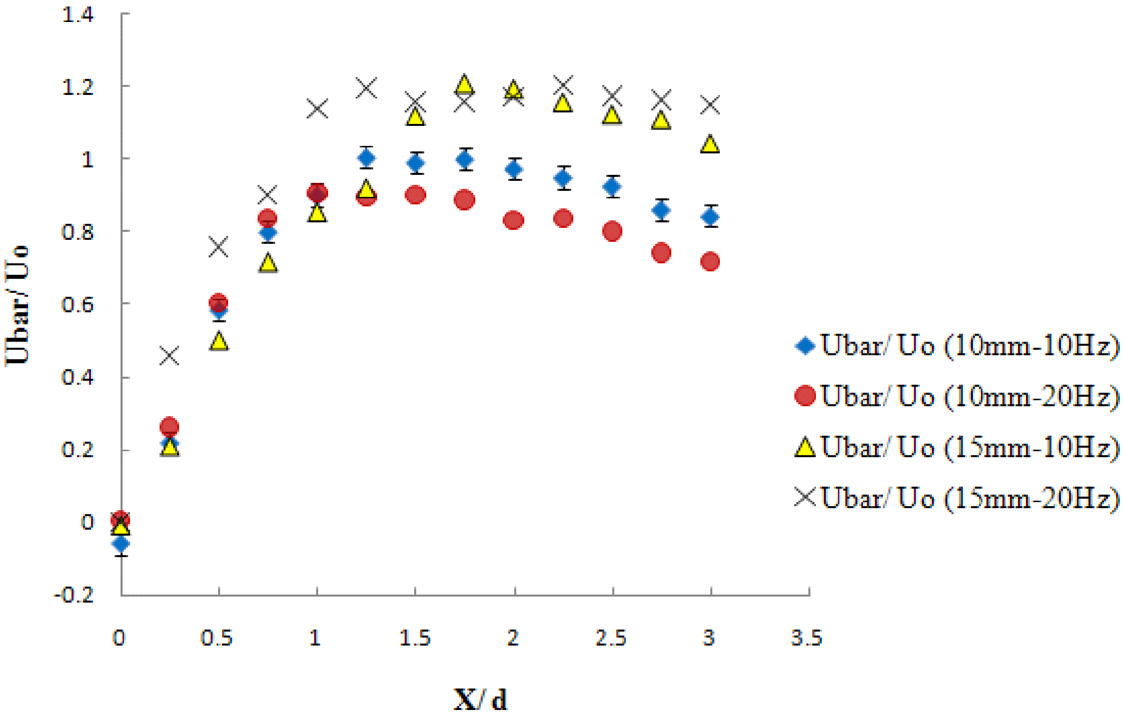

Figure 28 Time-averaged centerline velocity versus downstream distance from 0 to 3d with d/4 steps.

The flux volume of ejection must be theoretically equal to flux volume of suction and the U_{bar}/U_o is approximately zero at the orifice. The fact that these values are not zero is understandable as these readings only represent the values of velocity at the center of the orifice exit plane. The variation across the orifice exit plane from one case to another is responsible for the non-zero values. Of course the total volume flow rate into the chamber must still equal the total volume flow out of the chamber. As we traverse downstream on the centerline, the blowing effect is stronger than the suction and the U_{bar}/U_o increases. Beyond a certain distance (X/d $\simeq$ 1), the blowing phase has less effect and the U_{bar}/U_o begins to decrease. The data tend to drop sooner than Smith and Swift [1]. With perhaps the exception of the 15mm-20 Hz case, the data collapse well for X/d < 1. For values greater than X/d =1, the 15mm diameter cases are consistently greater than the 10 mm diameter cases. In the case of each diameter, there is not a consistent variation with frequency and its effect is smaller and is within the uncertainty.

The results follow the same trend as Smith and Swift [1]. Their results are shown in Figure 29. In order to make a comparison of the data easier; the obtained data in this study is plotted on a log scale in Figure 30. The legends in the figures show the Reynolds number and Stroke Length for each jet.

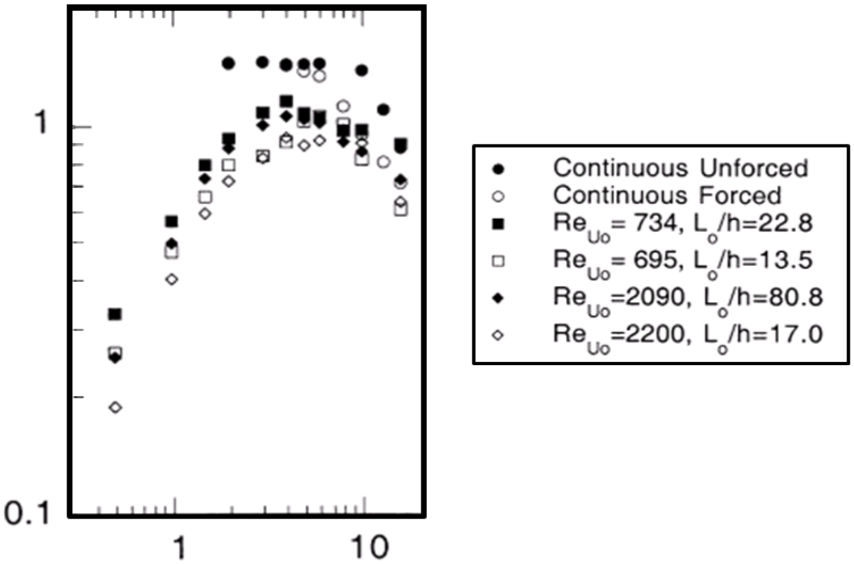

Figure 29 Smith and Swift results for time averaged centerline velocity versus downstream distances [1].

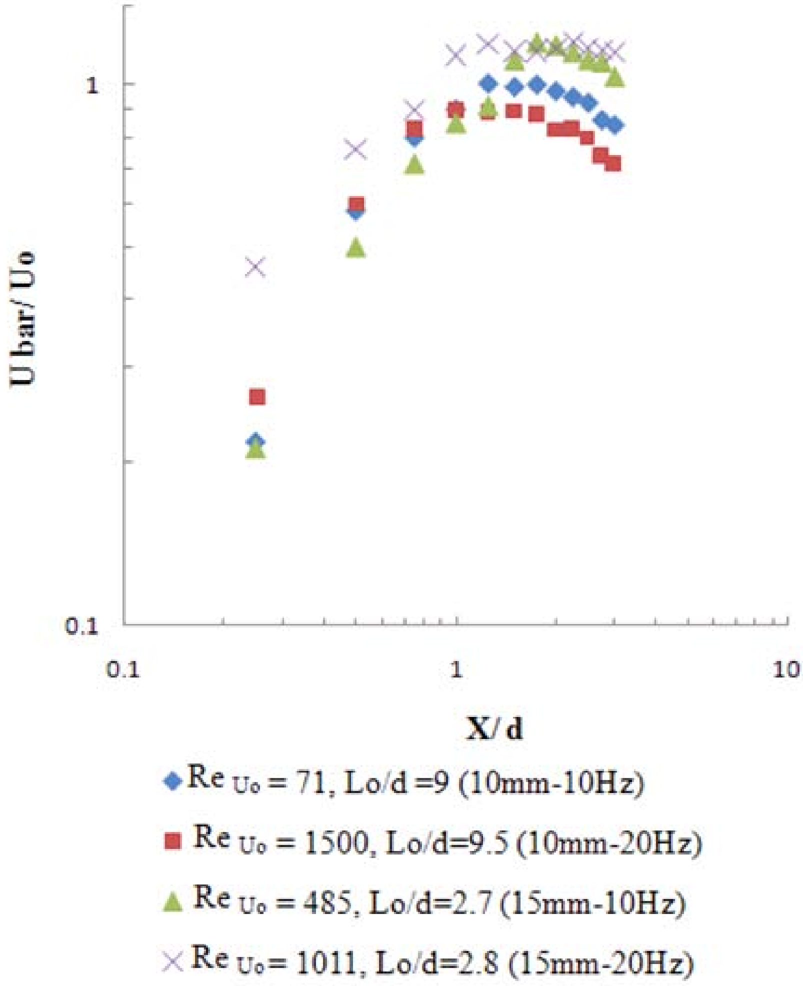

Figure 30 Experimental results, time averaged centerline velocity versus downstream distance (Log scale).

4.3 Velocity Profiles in the Radial Direction Study

The dimensionless velocity profiles in the radial direction are presented in Figure 31 and Figure 32 for axial downstream distances of d/2 and 11d/4 respectively. Error bars for one set of data are also included representing approximately 4% uncertainty in U/U_{cl} values (see Section A.9). In this case the time average velocity at each radius is normalized with respect to the centerline velocity. The dimensionless velocity profiles appear to be similar at X/d=11/4 but not at X/d=1/2.

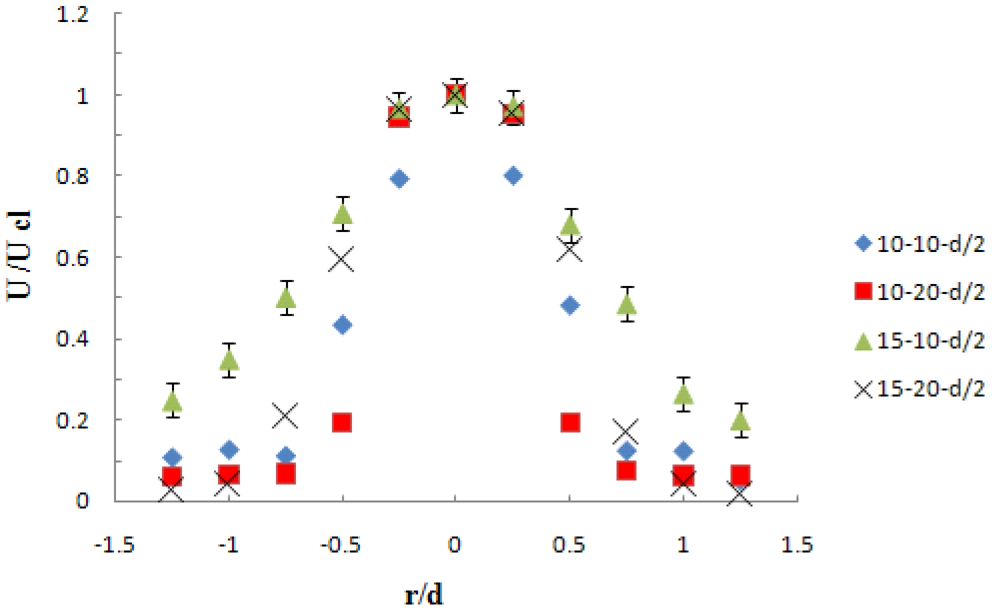

Figure 31 Mean velocity profile taken at d/2 distance downstream.

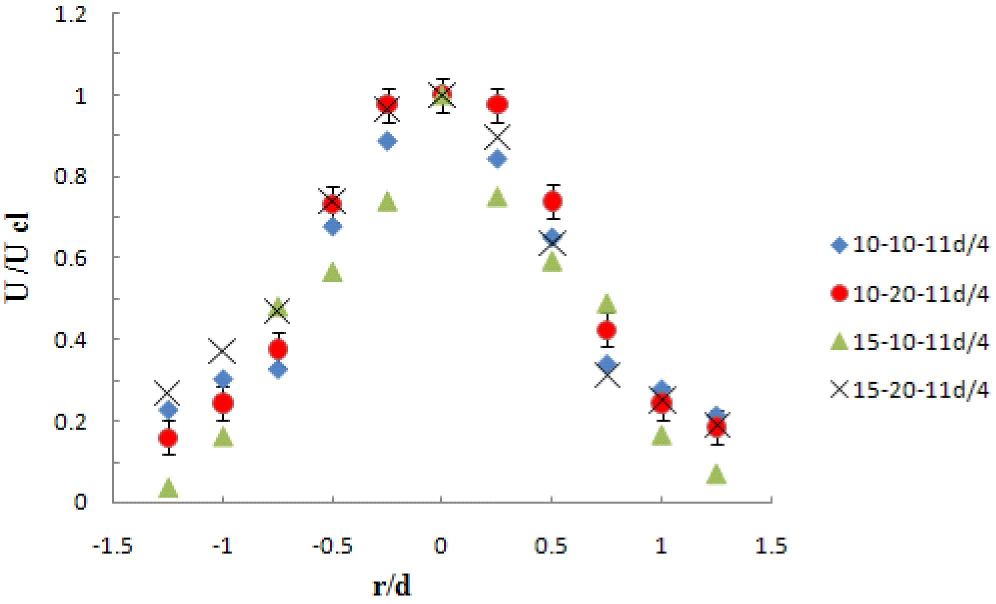

Figure 32 Mean velocity profile taken at 11d/4 distances downstream.

Jet width gives a quantitative measurement of the jet spreading. This value was determined by fitting a 4th order polynomial to the U/U_{cl} data versus r/d data in Figure 31 and Figure 32. The jet width (b) is taken as the radius at which the velocity is half of the centerline value. As seen in Figure 33, synthetic jets with larger Stroke Length, grow with a larger spreading rate. The jet width results are in good agreement with Smith and Swift [1]. Spreading ratio is found to be larger for the smaller diameter. Error bars are also demonstrated for one set of data estimating 4% uncertainty according to Section A.11.

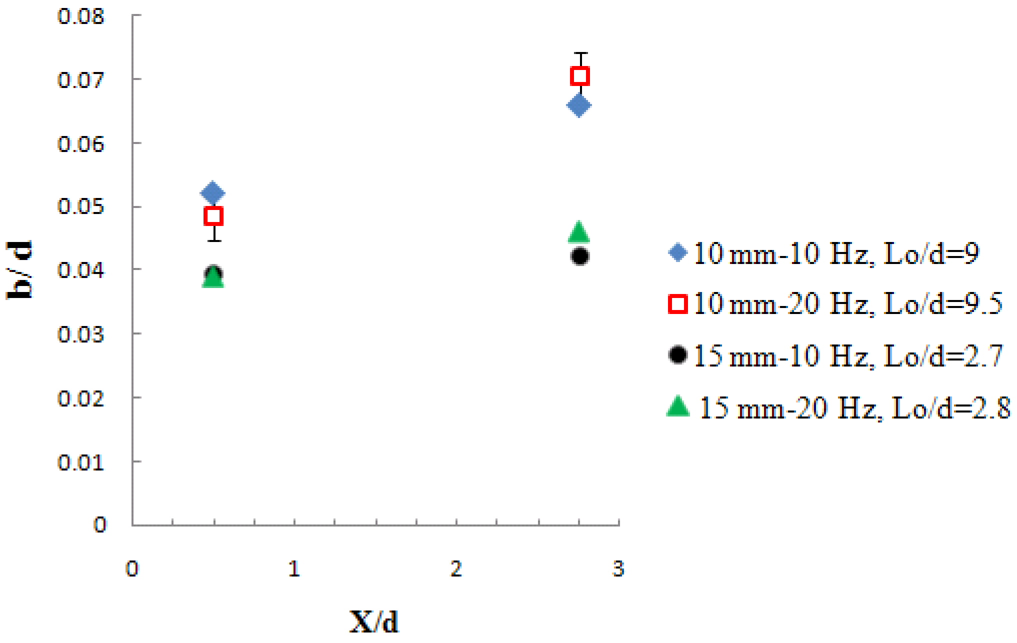

Figure 33 Jet width based on half maximum velocity as a function of downstream distance.

Chapter 5

CONCLUSIONS AND RECOMMENDATIONS

This chapter summarizes the important and relevant results obtained from this study and recommendations for future work.

5.1 Conclusions

1- A small variation of average velocity about zero is observed across the orifice exit plane.

2- The larger diameter orifice has less strength (power) than the smaller one. U_o values for the 15mm diameter jets were found to be 63% less than the 10 mm diameter jets at the same oscillating frequency.

3- A comparison for the same diameter jets shows that higher freque nncy causes stronger (more powerful) jets. U_o values for 20 Hz jets are 49% larger than 10 H jets.

4- Dimensionless parameters $\mathrm{U_{bar}/U_o}$ and X/d were capable of collapsing to a reasonable extent for the centerline velocity data in all cases.

5- Dimensionless velocity profiles along the centerline show the same trends as previous investigators such as Smith and Swift [1] and Smith and Glezer [7].

6- The dimensionless radial velocity profiles seem to be similar at X/d =11/4 but not at X/d=1/2.

7- Jet spreading is greater in the case of the smaller diameter orifice. It appears that dimensionless jet spread increases with L_o/d.

5.2 Recommendations

Possibilities for future work beyond the scope of this study include extension of the experimental measurements and investigation of the effect of different parameters such as diameter, radius curvature of the orifice, cavity volume and frequency range on the behavior of synthetic jets.

Another possibility is to study the higher Reynolds number jets and attain the transitional phase and turbulent phase behavior of the jet flow. Analyzing the rectified velocity curve could be an interesting and challenging study and better methods of overcoming the hot-wire directional ambiguity should be pursued.

The imposed effect of two synthetic jets on each other could also studied either experimentally or simulated numerically in order to find out the outcome power of a set of synthetic jets which could be useful in cooling or mixing applications.

APPENDICES

This section provides further information regarding the measurement procedures. A detailed uncertainty analysis can be found in Appendix A. Calibration and measurement procedure involving Thermal Pro software is briefly explained in Appendix B. This section can be used as a manual for future measurements with IFA300 CTA. The data measurements, analysis and plots can be found on the enclosed CD-ROM in Appendix C.

Appendix A: Uncertainty Analysis

Different variables such as velocity (U), frequency (*f*), Orifice diameter (d), the distance downstream from the orifice plane (X) and input signal voltage (V) are measured in this thesis. Multiple-measurement uncertainty analysis is assigned for the velocity measurements to quantify error estimates while single sample analysis is used for all other variables. The procedure for multiple-measurement uncertainty analysis separates elemental errors into bias (B) and precision (P) error [37]. The velocity measurement uncertainty (W_{u_o}) can be calculated as:

$$W_{u_o} = \sqrt{B^2 + (t_{\nu,95}\, P)^2} \tag{15}$$

where $t_{\nu,95}\, P$ is the estimate of the precision uncertainty in velocity measurements at a 95% confidence and ν degrees of freedom.

A.1 Bias in Velocity

Bias error for the multiple-measurement uncertainty analysis using hot-wire includes different sources of uncertainty such as, calibration equipment uncertainty, probe positioning, temperature variations and ambient pressure variation. For a general quantity reading, R, the uncertainty in the reading is defined as W_R and the relative uncertainty in the reading is the ratio of $\frac{W_R}{R}$. Bias is defined as the total relative uncertainty of readings from different error sources (i) shown as below [38].

$$W_{total} = 2.\sqrt{\sum_{i=1}^{n} {W_R}^2} \tag{16}$$

Each of these sources could reduce the measurement accuracy. Any change that causes the heat transfer from the wire into its surrounding is a disturbing factor [38]. Disturbing factors can be related to the flow medium or probe condition. Some important flow conditions that cause error are explained below.

Temperature variations drastically change the accuracy as the heat transfer is directly proportional to the difference of temperature between the sensor probe and the medium. The relative standard uncertainty in velocity measurements due to change in air temperature variations (W_{U_T}) is expressed as below [38].

$$W_{U_T} = \frac{1}{\sqrt{3}} \cdot \frac{\Delta T\ (°C)}{273} \tag{17}$$

ΔT is the difference between ambient reference temperature and the temperature during the measurements. For a wire probe used in air under normal conditions relative standard uncertainty in velocity measurements per 1°C change in temperature, is about 0.2% [38].

Ambient pressure variation changes the density and hence the velocity. The relative standard uncertainty in velocity measurements due to ambient pressure variation (W_{U_P}) is defined below. Typical value for ΔP is about 10 KPa [38].

$$W_{U_P} = \frac{1}{\sqrt{3}} \cdot \frac{P_{\mathrm{o}}}{P_{\mathrm{o}} + \Delta P} \tag{18}$$

where ΔP is differential pressure and P_o is standard pressure. The relative standard uncertainty in velocity measurements due to pressure variation for a 10 kPa, differential pressure is about 0.6% [38].

The misalignment of the probe in the calibration process and measurement process can affect the results. The probe holder in this case was aligned parallel to the flow perpendicular to the orifice plane. The relative standard uncertainty in velocity measurements due to probe misalignment ($W_{U_{positioning}}$) can be shown as [38]:

$$W_{U_{positioning}} = \frac{1}{\sqrt{3}} \cdot (1 - \cos\theta) \tag{19}$$

where θ is the degree of misalignment. Figure 34 shows θ in the probe positioning. A typical value for positioning a probe is 1° and the relative standard uncertainty in velocity measurements due to probe misalignment is approximately zero [38].

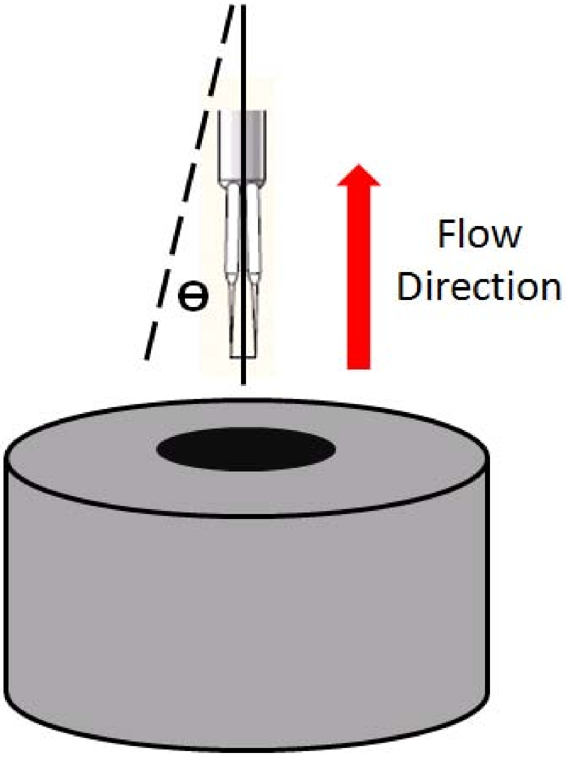

Figure 34 Misalignment degree (θ).

Calibration uncertainty could be a major source of error in the experiment. Calibration uncertainty can be shown as below, $\mathrm{a_{cal}}$ is a relative standard uncertainty and $\mathrm{b_{cal}}$ is a constant contribution. $\mathrm{b_{cal}}$ can only be neglected for velocities over 5 m/s [38].

$$\mathrm{STDV(U_{calibrator})} = \mp \mathrm{a_{cal}}(\%) + \mathrm{b_{cal}}(\mathrm{m/s}) \tag{20}$$

Usually $\mathrm{a_{cal}}$ is ∓ 0.01 and $\mathrm{b_{cal}}$ is ∓ 0.02. The relative standard uncertainty due to calibration equipment error is:

$$W_{U_{calibrator}} = \frac{1}{100} . \mathrm{STDV(U_{calibrator}(\%))} \tag{21}$$

According to the air calibrator manual [38] accuracy of the velocity reading is approximately 0.5% which is valid since it is in the acceptance range:

$$-3\% \ll W_{U_{calibrator}} \ll 3\% \tag{22}$$

Total relative uncertainty (W_{total}) can be calculated using the following formula:

$$W_{total} = 2.\left({W_{U_T}}^2 + {W_{U_P}}^2 + {W_{U_{calibrator}}}^2 + {W_{U_{positioning}}}^2 \right)^{1/2} \quad (23)$$

Total relative uncertainty in this case is calculated to be ∓ 0.016.

A.2 Precision in Velocity

Since a number of cycles are over layered on one cycle, velocity difference appears in the form of a band. Figure 35 shows the velocity range on a set of data taken at the center of the 10 mm diameter orifice at 10 Hz. The solid line shows 33 cycles of data points over layered on one period. A Fourier Series is used to fit the data and gives an estimate of the mean value of the measured velocities which is used to correct the rectified curve. The dashed line shows the directional ambiguity corrected Fourier fitted curve. The velocity values for all cycles and the mean values at t=0 and t=$\frac{T}{2}$ for 10-10-0-0 are shown in Figure 36. The velocities are plotted starting from 2.9 m/s instead of 0 m/s for presentation purposes.

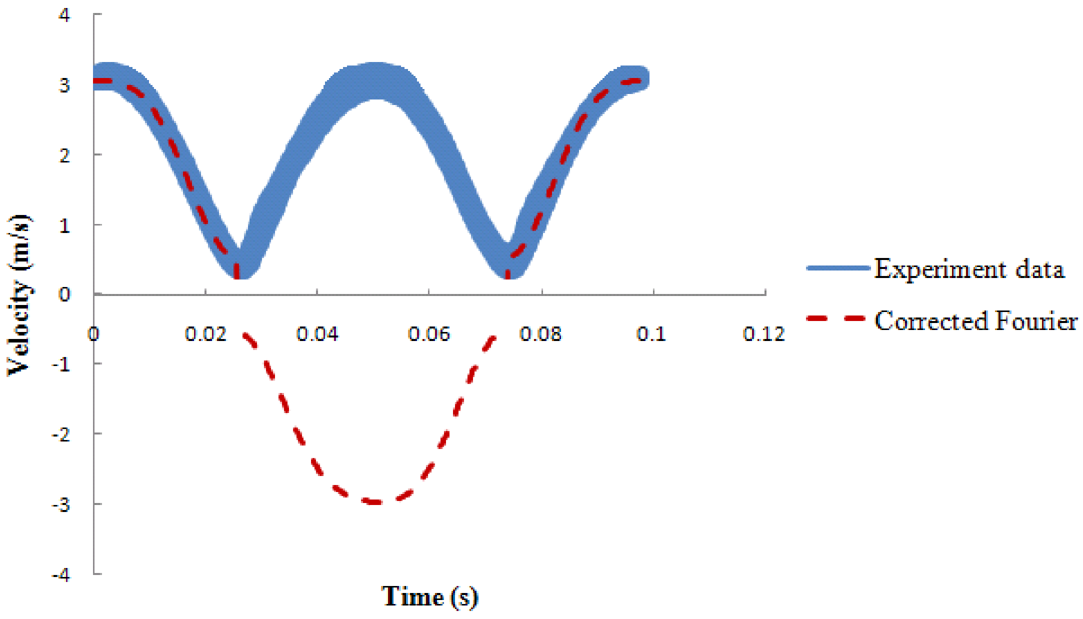

Figure 35 Phase locked data and Fourier fitted curve for 10-10-0-0.

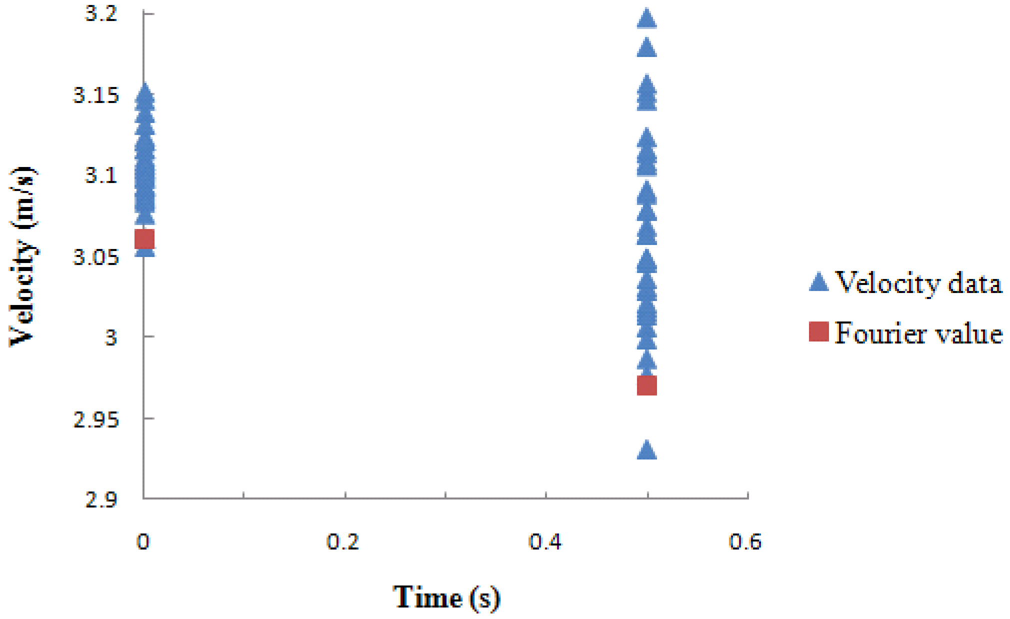

Figure 36 Velocity values at t=0 and t= $\frac{T}{2}$ for 10-10-0-0.

In order to calculate the multiple sampling uncertainties, the precision of the measurements must be estimated. The sample standard deviation for a sample of $u_o(t)$ data points (STD) is used to estimate the precision (P) of the measurements and is shown below:

$$\mathrm{P} = \sqrt{\frac{1}{N-1}\sum_{i=1}^{N} \left[(u_o(t))_i - \bar{u}\right]^2} \tag{24}$$

where N is number of data points and $\bar{u}$ is the averaged velocity of a sample measurement over one cycle. Since Fourier Series is used to provide a mean value for the entire number of cycles, for instance in the 10 Hz measurement 33 cycles, the Fourier mean value is used. This value is almost the same as the mean value calculated using the following formula:

$$\bar{u} = \frac{1}{N}\sum_{i=1}^{N}(u_o(t))_i \tag{25}$$

Calculation of *P* shows an approximate uncertainty of ∓ 0.114 m/s in the velocity measurements due to the precision. The estimate of the precision uncertainty in velocity measurements at a 95% confidence is defined by $t_{\nu,95}P$ [37].

$t_{\nu,95}$ is extracted from the "Student *t* Distribution" table [37] where degrees of freedom (ν) is defined as given below:

$$\nu = M - 1 \tag{26}$$

where *M* is the number of finite measurement cycles of velocity. At 10 Hz, for each sampling measurement, *M* is 33 cycles which means at a 95% confidence and a 32 degrees of freedom, $t_{\nu,95}$ is 2.037. The measurement uncertainty in velocity due to the precision is calculated to be 0.232 m/s which gives a relative uncertainty of $\mp$ 0.078.

A.3 Velocity Uncertainty

Using the bias and precision previously determined, the overall relative uncertainty in velocity measurements is $\mp$ 0.08.

A.4 Diameter Measurement Uncertainty

Orifice diameters are measured using a vernier caliper which provides the resolution of $\mp$ 0.025 mm. The zero-order uncertainty of the caliper ($W_{caliper}$) with a probability of 95% is calculated using Equation 27 and resulted in a $\mp$ 0.0125 mm of error in reading the diameter of the orifice. For the 10 mm diameter orifice this becomes as a percentage of 0.125%.

$$W_{caliper} = \mp\frac{1}{2}\ resolution \tag{27}$$

A.5 Frequency Measurement Uncertainty

Since frequency and period are related inversely, period can be used to estimate the amount of error in the frequency measurements. Standard deviation in period measurements for 10-10-0-0 case is calculated as:

$$W_{Period} = \sqrt{\frac{1}{M-1}\sum_{i=1}^{M}\ [(T)_i - \bar{T}]^2} \tag{28}$$

where $\bar{T}$ is the mean value of period over the whole number of samples. $\bar{T}$ is calculated to be 0.0991 seconds for 10-10-0-0 case. The period of each cycle is shown by $(T)_i$, i is the number of the cycle. W_{Period} is almost zero ($5.9 \times 10^{-5}\ s$). Input signal frequency uncertainty can be determined to be $\mp$ 0.006 Hz using Equation 29. For the 10 Hz case this becomes 0.06% .

$$W_{frequency} = f\,\frac{W_{period}}{T} \tag{29}$$

A.6 Input Signal Voltage Measurement Uncertainty

Input voltage could be measured using an oscilloscope. The zero-order uncertainty [37] in setting the voltage is calculated using Equation 30 which resulted in a ∓ 0.1 Volts of error. For an input voltage of 8 volts this represents 1.25%.

$$W_{voltage} = \mp \frac{1}{2}\, resolution \tag{30}$$

A detailed uncertainty analysis of the velocity measurements is conducted in this section of the thesis. The summary of this analysis is shown in Table 8.

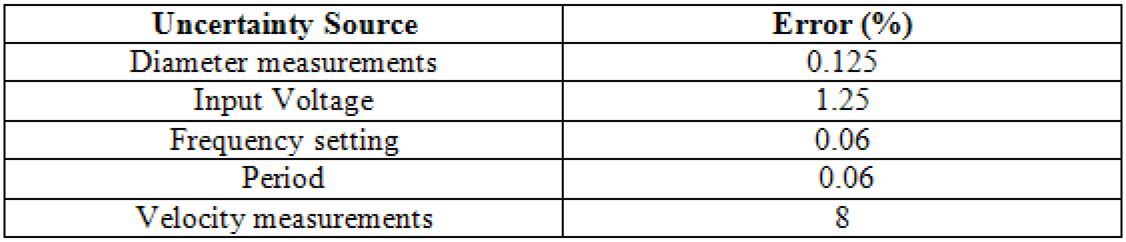

Uncertainty Source	Error (%)
Diameter measurements	0.125
Input Voltage	1.25
Frequency setting	0.06
Period	0.06
Velocity measurements	8

Table 8 Uncertainty analysis results.

A.7 U_{bar} and U_o Uncertainty

U_{bar} and U_o are determined in this thesis by integration of Fourier Series. Since an estimation of the uncertainty of the Fourier Series is extremely complicated, an alternate method is used. The definition of U_{bar} is used instead. According to Equation 6, U_{bar} can be approximated as a summation of velocity points at time intervals of Δt. Equations 31 and 32 show Δt and U_{bar}.

$$\Delta t = \frac{T}{N} \tag{31}$$

$$U_{bar} = \frac{1}{N\,\Delta t}\sum_{i=1}^{N} U_i\,\Delta t \tag{32}$$

Since Δt is constant it can be cancelled from the Equation 32. Equation 33 shows the uncertainty of U_{bar} ($W_{U\,bar}$).

$$W_{U\,bar} = \frac{1}{N}\sum_{i=1}^{N} \sqrt{\left(\frac{\partial U_{bar}}{\partial U_i}\,W_{U\,i}\right)^2}$$

$$= \sqrt{\left(\frac{\partial U_{bar}}{\partial u_2}W_{u_2}\right)^2 + \left(\frac{\partial U_{bar}}{\partial u_2}W_{u_2}\right)^2 + \cdots + \left(\frac{\partial U_{bar}}{\partial u_N}W_{u_N}\right)^2} \tag{33}$$

which results in Equation 34.

$$W_{U_{bar}} = \frac{1}{N}\sqrt{N\,{W_u}^2} = \frac{1}{\sqrt{N}}W_u \qquad (34)$$

Similarly, the uncertainty in U_o can also be shown to be :

$$W_{U_o} = \frac{2}{\sqrt{N}}W_u \qquad (35)$$

In the 20 Hz case with 250 data points, $W_{U_{bar}}$and $W_{U_o}$are calculated as 0.005 m/s and 0.01 m/s Uncertainty of $\frac{U_{bar}}{U_o}$ can be determined by Equation 36.

$$\frac{W_{U_{bar}/U_o}}{U_{bar}/U_o} = \sqrt{(\frac{W_{U_{bar}}}{U_{bar}})^2 + (\frac{W_{U_o}}{U_o})^2} \qquad (36)$$

By replacing $W_{U_{bar}}$and $W_{U_o}$with their values from Equations 34 and 35 and also considering $U_{bar} = 0.169$ m/s and U_o =1.894 m/s for the 10mm-20 Hz case, $\frac{W_{U_{bar}/U_o}}{U_{bar}/U_o}$ can be calculated to be 0.03.

A.8 Uncertainty in Traverse Positioning

Zero setting the traverse is done visually. It can be claimed by the author that zero setting in X direction can be done with 95% confidence at $\mp \frac{d}{20}\,(W_X)$ which is 0.5 and 0.75 mm for the 10 and 15 mm diameter orifice, however in the Y direction, it can be done with 95% confidence at $\mp \frac{d}{16}\,(W_y)$ which is 0.62 and 0.93 mm for the 10 and 15 mm diameter orifice.

$$W_{X/_d} = \sqrt{(\frac{W_X}{X})^2 + (\frac{W_d}{d})^2} \tag{37}$$

W_d is the orifice diameter measurement uncertainty explained in Section A.4 and X is the distance from the center of the orifice downstream. The second term of the Equation 37 is negligible, therefore; $W_{X/_d}$ is calculated to be 0.0016 at X=d/4 in 10mm case.

A.9 Uncertainty in $U/_{U_{cl}}$

In order to find uncertainty of $W_{U/_{U_{cl}}}$, it should be considered that equals the value of U_{bar} at $r/d = 0$. Equation 38 used to calculate the relative uncertainty of $U/_{U_{cl}}$which resulted in a value of $\mp$ 0.042.

$$\frac{W_{U/U_{cl}}}{U/U_{cl}} = \sqrt{(\frac{W_U}{U})^2 + (\frac{W_{U_{cl}}}{U_{cl}})^2} \qquad (38)$$

A.10 Uncertainty in r/d

The relative uncertainty in r/d can be calculated using Equation 39. r is the jet width and W_r/r is the relative uncertainty of jet width which is observed from the curves to be nearly 0.03.

$$\frac{W_{r/d}}{r/d} = \sqrt{(\frac{W_r}{r})^2 + (\frac{W_d}{d})^2} \qquad (39)$$

The second term can be neglected since W_d itself is small. The relative uncertainty is then calculated to be $\mp$.0.03.

A.11 Uncertainty in b/d

$W_{b/d}$ values are estimated to be $\mp$ 0.04 by looking directly at the difference between the curve fitted data and the data points at U/U_{cl} = 0.5. For a b/d value of 0.4, $\frac{W_{b/d}}{b/d}$ is then calculated to be $\mp$ 0.1.

Appendix B: Calibration and Data Acquisition using Thermal Pro Software

Measuring with a hot-wire needs specific configuration and settings. Many options can be found on each screen which makes it necessary to understand and evaluate the best choice to use for measuring procedure. This section includes more detailed and sequential guidelines for calibration, acquisition and analysis associated with hot-wire anemometry. This information along with the software and hardware manual of IFA300 should be used to overcome the complexity of the software.

B.1 Hot-wire Anemometry Calibration Procedure

Calibration is an important step in every measurement procedure. In this experiment the measuring probe is the device that should be calibrated. An automated air velocity calibrator (TSI Model 1129) is used to calibrate the single-sensor probe.

To calibrate the probe, there are certain steps that need to be taken as listed below:

1- Choose the correct secondary and primary nozzle according to the velocity range of the study. In this study the desired velocity calibration range is from 0 to 5 m/s and hence a secondary nozzle with 14 mm diameter and differential pressure range between 0.4 to 100 mmHg is chosen with the primary nozzle number 3 of the TSI automated air velocity calibrator (Figure 37).

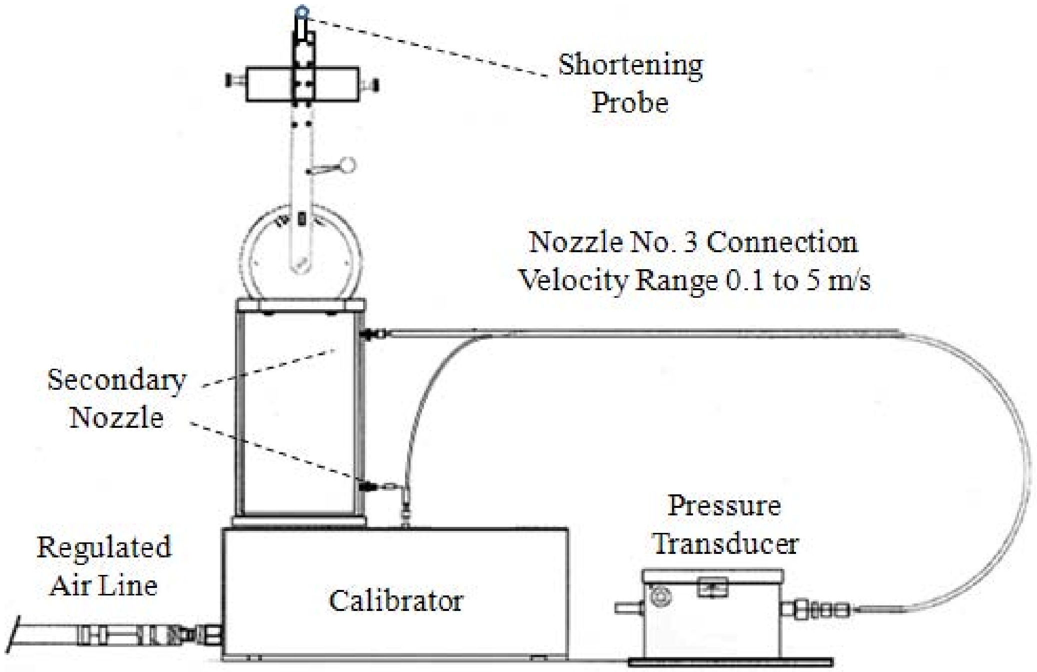

Figure 37 Automated air calibrator used to calibrate the probe [36].

2- Measure the resistance of the probe cable using a shortening probe. In this study, a 5 meter cable is used to attach the probe holder and the Channel 1 port on IFA300. In the calibration-probe data, the resistance of the cable can be measured by selecting the “Read” button. For a 5 meter cable the resistance is measured to be 0.36 Ω (Figure 38).

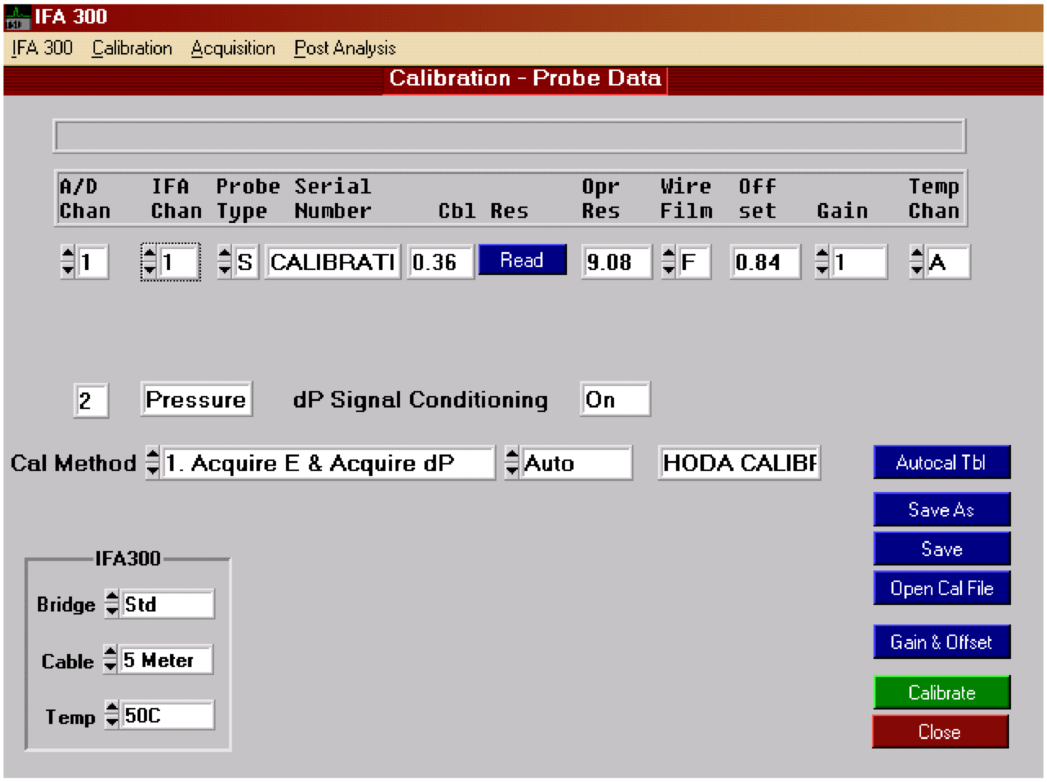

A/D Chan	IFA Chan	Probe Type	Serial Number	Cbl Res	Opr Res	Wire Film	Off set	Gain	Temp Chan
1	1	S	CALIBRATI	0.36	9.08	F	0.84	1	A

2 Pressure dP Signal Conditioning On

Cal Method 1. Acquire E & Acquire dP Auto HODA CALIBF

IFA300
Bridge Std
Cable 5 Meter
Temp 50C

Figure 38 Calibration-probe data screen.

3- Install the measuring probe. Probes are fragile and should be handled cautiously. The probe should only be installed while the CTA is on stand-by or while the power is disconnected.

4- Gain and offset values must be calculated and applied to bridge voltage. The main reason to apply these two values is to assure that the output voltage is as close as possible to the DC voltage span of the A/D board, which is between -5 to +5. Gain and offset can be calculated automatically choosing the “Calibrate” button on the calibration-probe data screen (Figure 38) or manually using the following formulae [36]:

Offset can be determined by:

$$\text{Offset} = \frac{1}{2}(\text{Bridge Voltage}_{\text{max}} + \text{Bridge Voltage}_{\text{min}}) \quad (40)$$

Gain range can be determined by:

$$[-4 \div (\text{Bridge Voltage}_{\text{min}} - \text{Offset})] \geq \text{Gain} \leq [4 \div (\text{Bridge Voltage}_{\text{max}} - \text{Offset})] \quad (41)$$

The relation between the output voltage and the bridge voltage is:

$$\text{Output Voltage} = [\text{Bridge Voltage} - \text{Offset}] \times \text{Gain} \quad (42)$$

In this experiment, Gain and Offset were calculated to be 12 and 1.52 volts respectively. Figure 39 shows the Gain and Offset calculator. Probe type, high flow and low flow velocity values must be entered. By selecting “Acquire”, pressure is set by the pressure transducer and by selecting “Calculate” Thermal Pro software calculates Gain and Offset using formulae 31, 32 and 33.

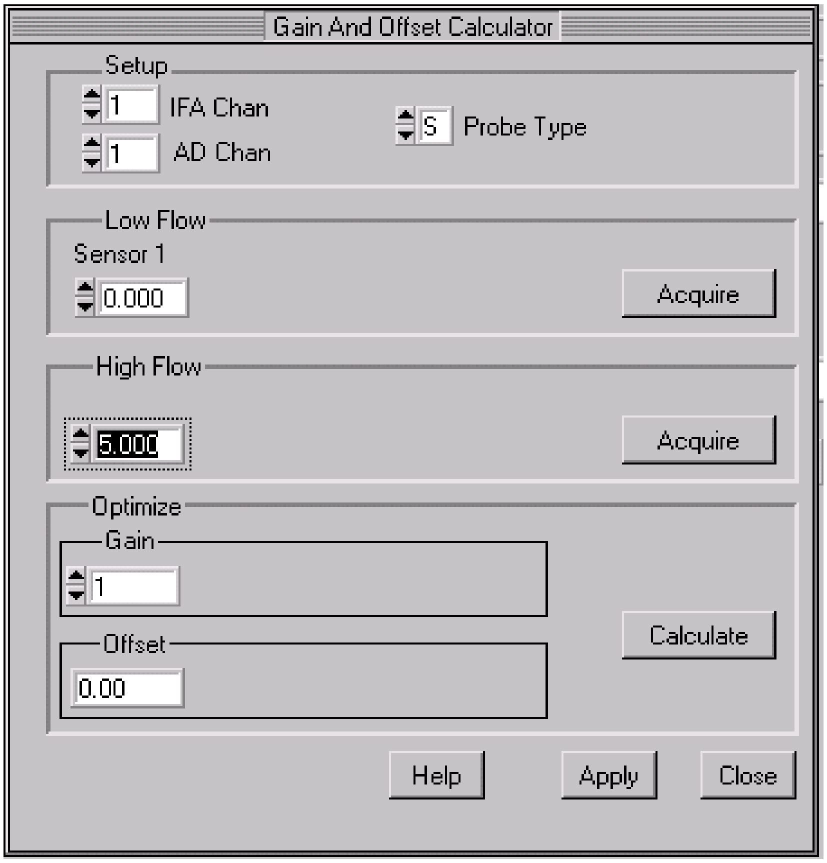

Gain And Offset Calculator

Setup

1 IFA Chan

1 AD Chan

S Probe Type

Low Flow

Sensor 1

0.000

High Flow

5.000

Optimize

Gain

1

Offset

0.00

Figure 39 Gain and offset calculator.

5- The calibration points in the calibration-data table (Figure 40) are defined, by entering the minimum and maximum velocity, temperature and atmospheric pressure. The Thermal Pro software calculates the required calibration points for the selected velocity range. There are 17 points used for the calibration. Approximately 2/3 of the points are in the lower 25% of the velocity range. The velocity of each point and required differential pressure for each point are shown in the calibration-data table (Figure 40).

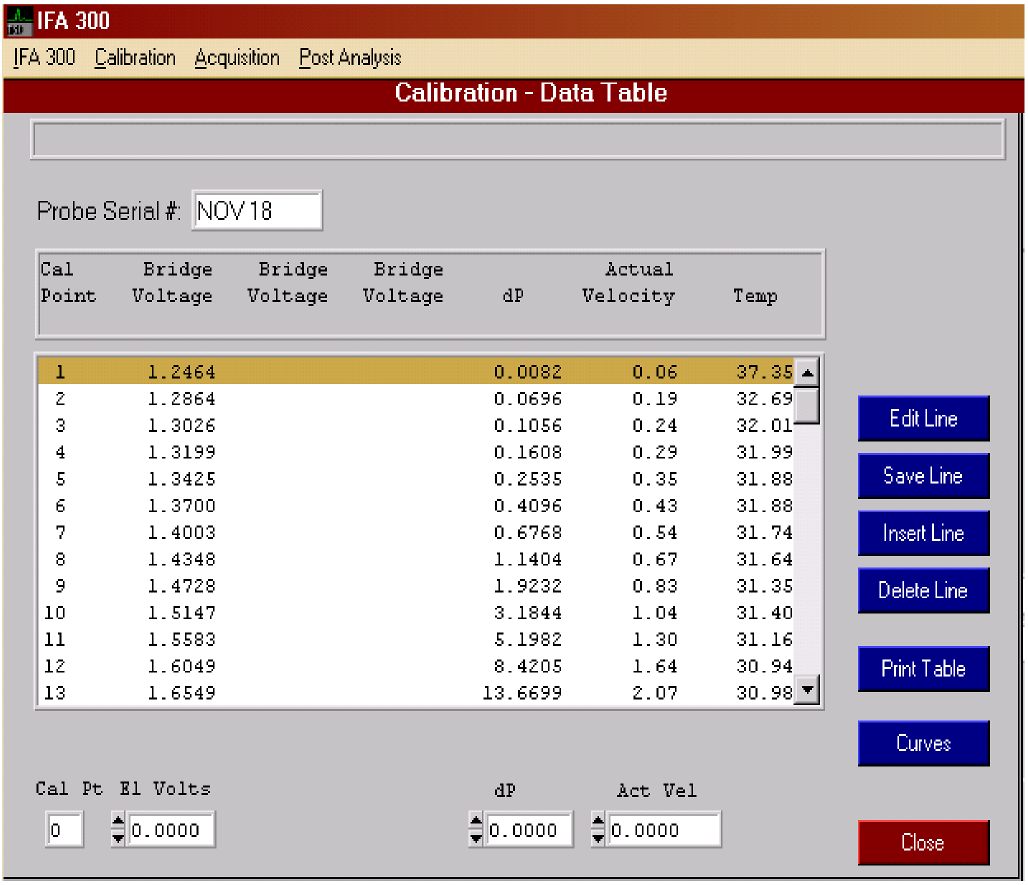

Probe Serial #: NOV 18

Cal Point	Bridge Voltage	Bridge Voltage	Bridge Voltage	dP	Actual Velocity	Temp
1	1.2464			0.0082	0.06	37.35
2	1.2864			0.0696	0.19	32.69
3	1.3026			0.1056	0.24	32.01
4	1.3199			0.1608	0.29	31.99
5	1.3425			0.2535	0.35	31.88
6	1.3700			0.4096	0.43	31.88
7	1.4003			0.6768	0.54	31.74
8	1.4348			1.1404	0.67	31.64
9	1.4728			1.9232	0.83	31.35
10	1.5147			3.1844	1.04	31.40
11	1.5583			5.1982	1.30	31.16
12	1.6049			8.4205	1.64	30.94
13	1.6549			13.6699	2.07	30.98

Cal Pt: 0
El Volts: 0.0000
dP: 0.0000
Act Vel: 0.0000

Figure 40 Calibration-data table.

6- The next step is the acquisition of the calibration points (Figure 41). On the calibration condition setup screen, calibration points and calibration curve can be acquired by selecting “Acquire” button. The resulting calibration points are shown on Figure 42. In the next screen (Figure 43), a curve fitting method is applied to the calibrated points. Different fitting methods can be chosen such as King’s law or polynomial with the option of choosing the order. A curve fitted result is shown in Figure 43. A 5th order polynomial gives an acceptable fitting. The probe is now ready to be used for measurements.

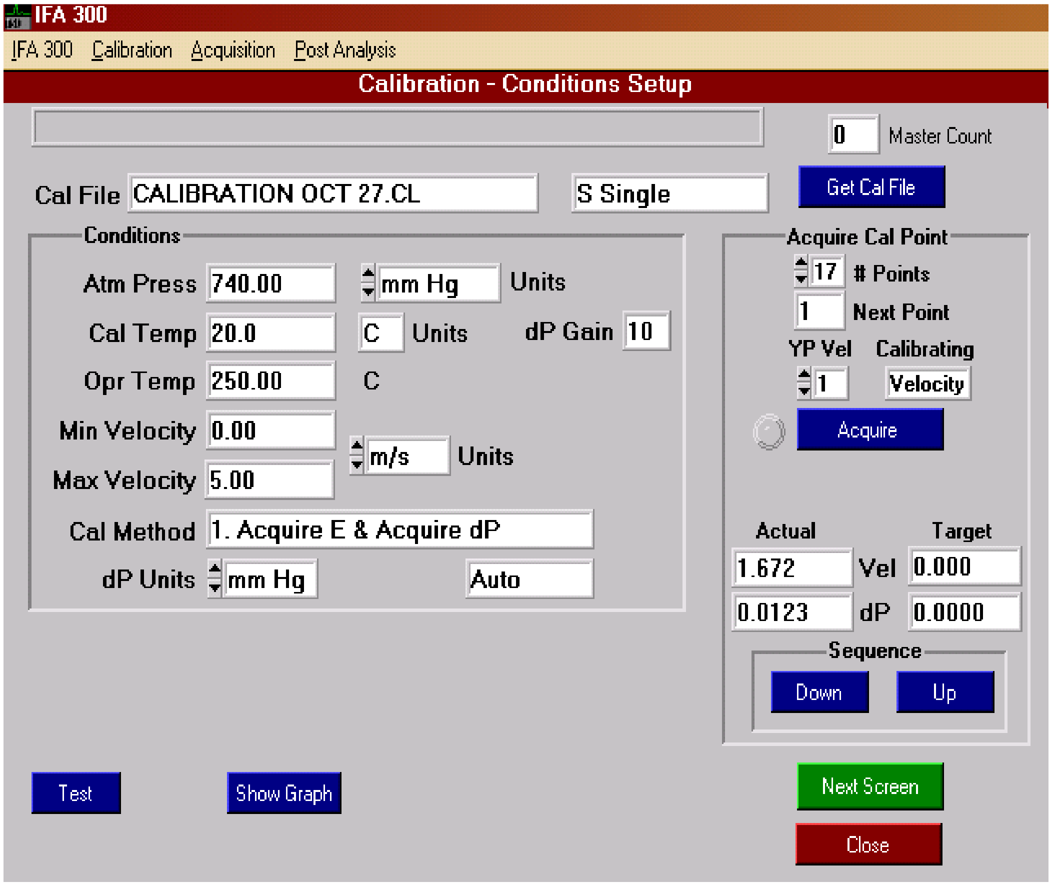

Master Count: 0

Cal File: CALIBRATION OCT 27.CL — S Single

Conditions

Atm Press: 740.00 — mm Hg Units

Cal Temp: 20.0 — C Units — dP Gain: 10

Opr Temp: 250.00 — C

Min Velocity: 0.00

Max Velocity: 5.00 — m/s Units

Cal Method: 1. Acquire E & Acquire dP

dP Units: mm Hg — Auto

Acquire Cal Point

17 # Points

1 Next Point

YP Vel: 1 — Calibrating: Velocity

	Actual	Target
Vel	1.672	0.000
dP	0.0123	0.0000

Figure 41 Calibration-condition setup.

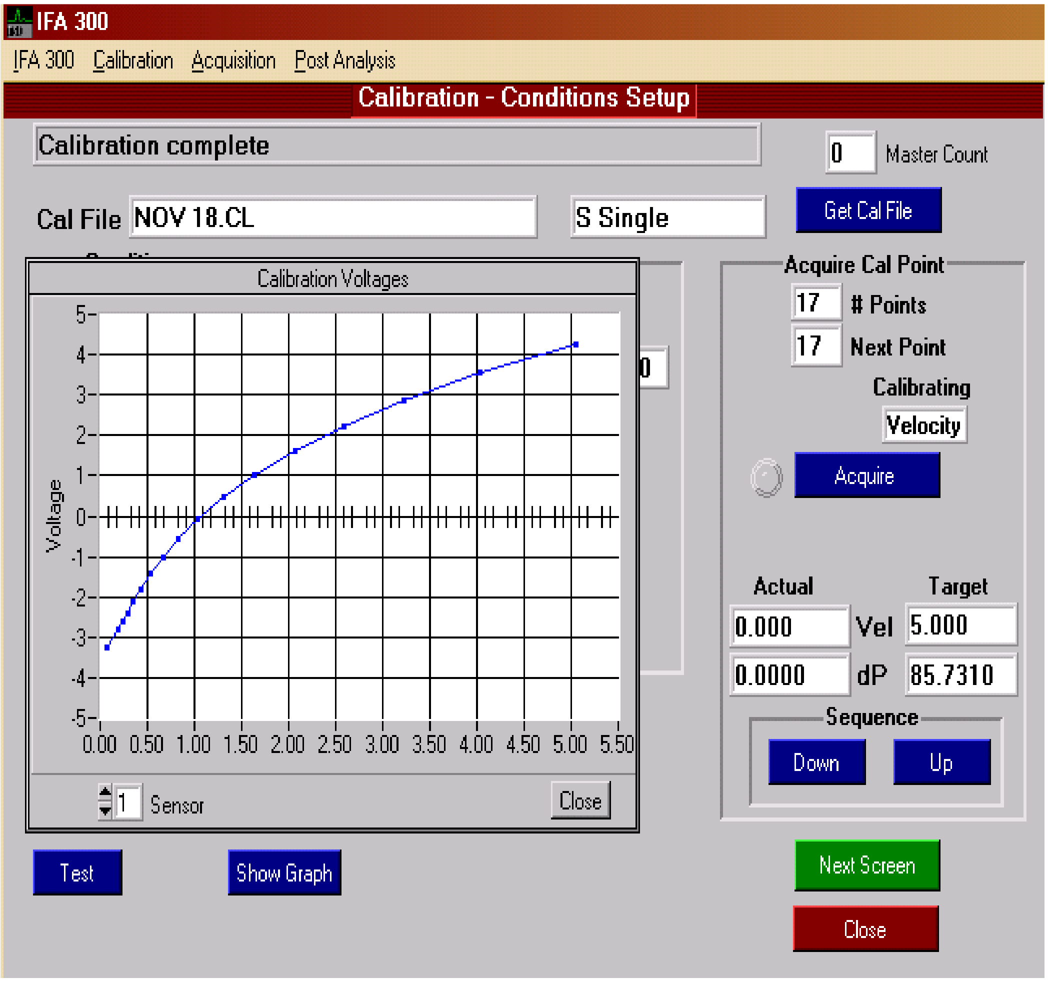

Calibration complete

Master Count: 0

Cal File: NOV 18.CL

S Single

\# Points: 17

Next Point: 17

Calibrating: Velocity

Sensor: 1

	Actual	Target
Vel	0.000	5.000
dP	0.0000	85.7310

Figure 42 Acquired calibration points.

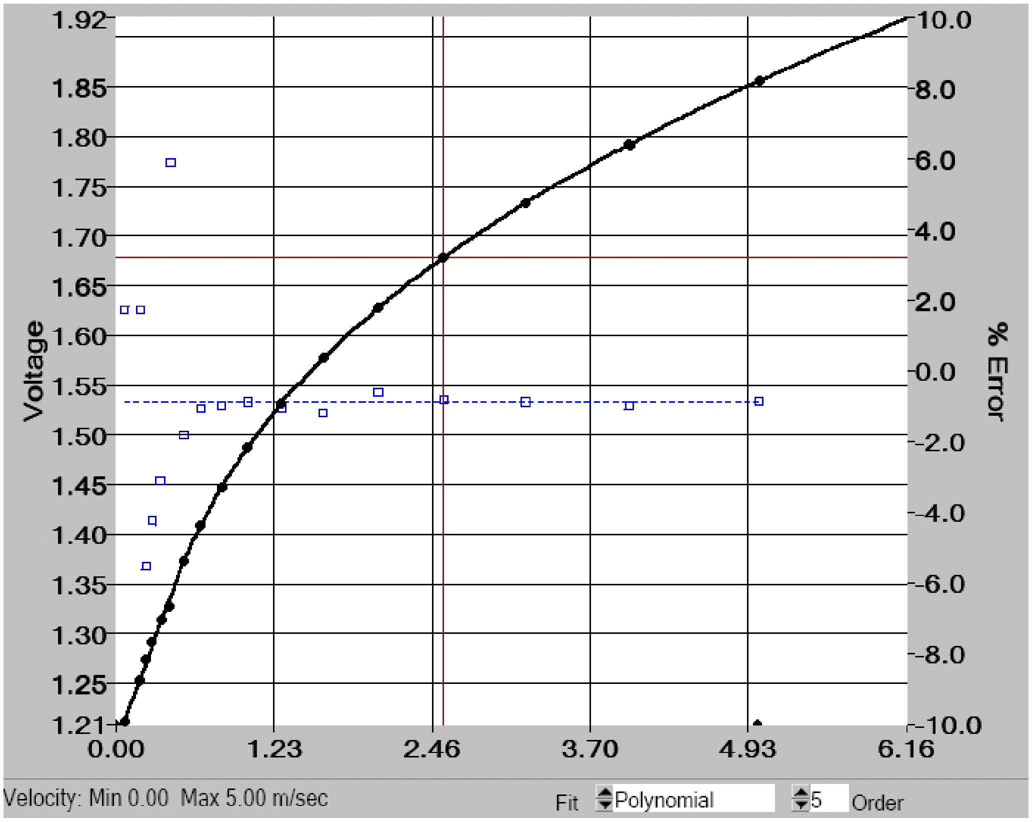

Velocity: Min 0.00 Max 5.00 m/sec

Fit Polynomial 5 Order

Figure 43 Calibration curve fitting screen.

B.2 Hot-wire Anemometry Measurement Procedure

The hot-wire probe must be positioned in the desired place before data sampling. The traverse is used to locate the probe at the desired position. Thermal Pro software provides a controller for the traverse. Figure 44 shows the traverse controller table. Traverse can be controlled by setting the controller either on remote control (software) or local control (remote control device).

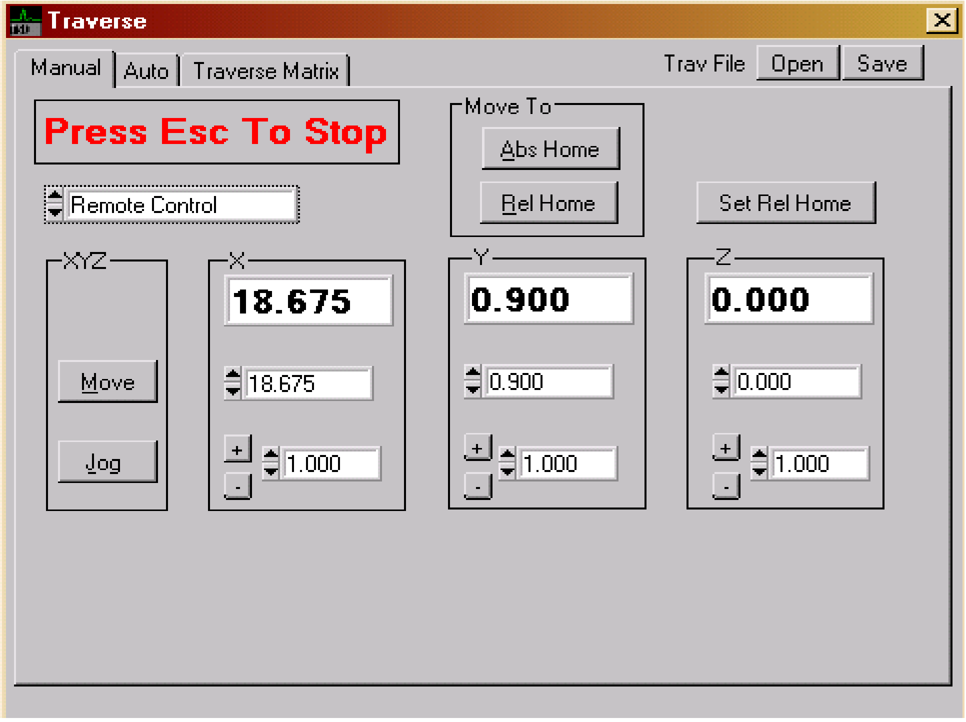

Remote Control

X: 18.675, 18.675, 1.000

Y: 0.900, 0.900, 1.000

Z: 0.000, 0.000, 1.000

Figure 44 Traverse control table.

The resistance of the calibrated probe must be measured before each measurement. There are three channels used out of 8 available channels on the TSI D/A acquisition board. Channel 1 is connected to the output voltage of the IFA300, Channel 2 is connected to the pressure transducer output and Channel 3 is linked to the function generator output. Figure 14 of the thesis shows the TSI board with the connections.

After orienting the probe in the desired spot, data acquisition can be started. On the “Acquisition-probe data” screen (Figure 45), Channel number 1 is automatically chosen. For the other channels, additional probes can be added using the “Add probe” button. Each probe line can be edited using the “Edit Line” button. After adding each probe line, it must be saved.

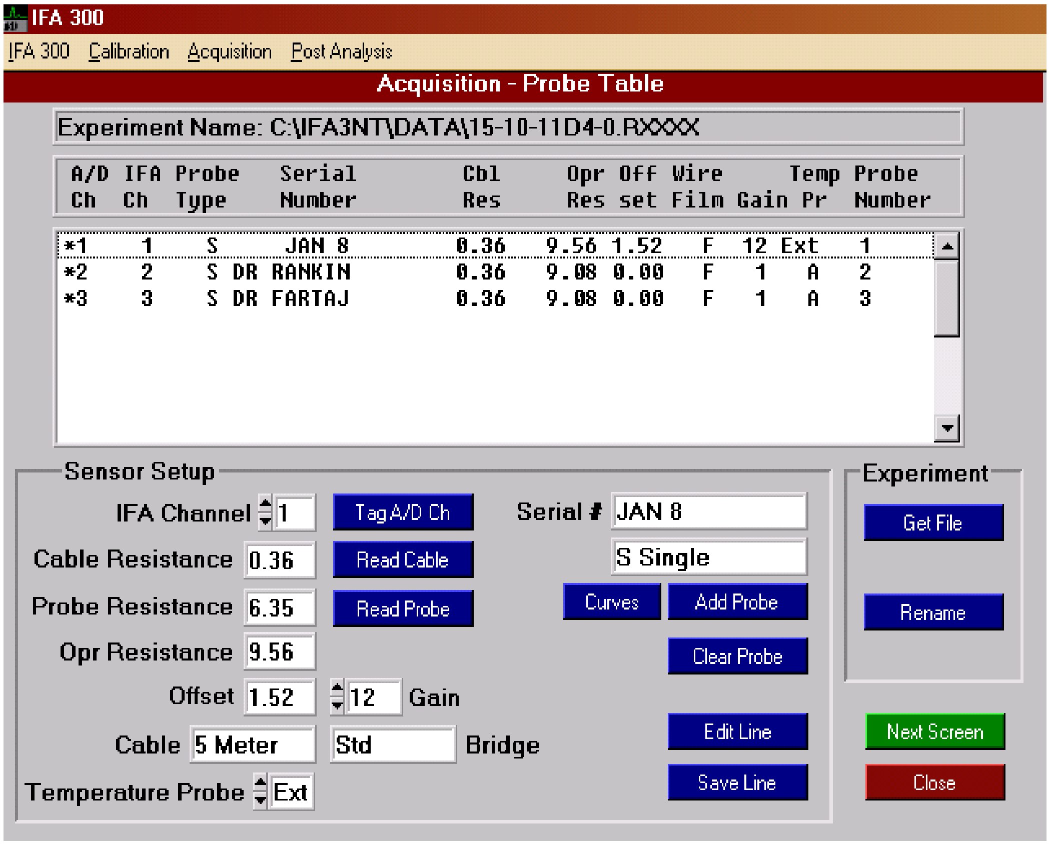

Experiment Name: C:\IFA3NT\DATA\15-10-11D4-0.RXXXX

```
A/D IFA Probe    Serial          Cbl      Opr  Off  Wire      Temp Probe
Ch  Ch  Type     Number          Res      Res  set  Film Gain Pr   Number

*1    1    S      JAN 8         0.36    9.56 1.52    F   12 Ext    1
*2    2    S  DR RANKIN         0.36    9.08 0.00    F    1   A    2
*3    3    S  DR FARTAJ         0.36    9.08 0.00    F    1   A    3
```

IFA Channel 1

Cable Resistance 0.36

Probe Resistance 6.35

Opr Resistance 9.56

Offset 1.52

12 Gain

Cable 5 Meter

Std Bridge

Temperature Probe Ext

Serial # JAN 8

S Single

Figure 45 Acquisition-probe data.

Once all the parameters are entered and probe resistance is measured, the next screen (Figure 46) allows a choice of the sampling rate, number of points, atmospheric pressure and measuring units. Choosing sample rate and number of points, the total time is calculated by the software. The measuring trigger (Figure 46) is chosen to be an internal one. This screen also allows the experiment to be named with the "Rename" button.

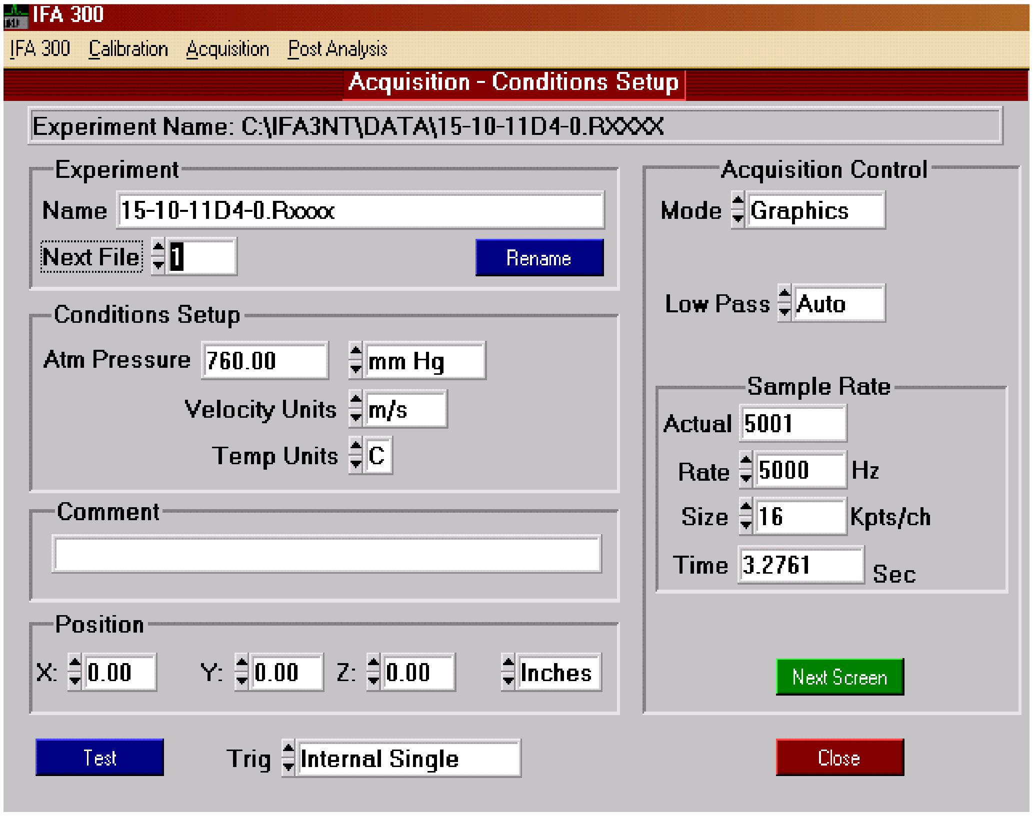

Acquisition - Conditions Setup

Experiment Name: C:\IFA3NT\DATA\15-10-11D4-0.RXXXX

Experiment

Name 15-10-11D4-0.Rxxxx

Next File 1

Conditions Setup

Atm Pressure 760.00 mm Hg

Velocity Units m/s

Temp Units C

Comment

Position

X: 0.00 Y: 0.00 Z: 0.00 Inches

Acquisition Control

Mode Graphics

Low Pass Auto

Sample Rate

Actual 5001

Rate 5000 Hz

Size 16 Kpts/ch

Time 3.2761 Sec

Trig Internal Single

Figure 46 Acquisition-condition setup.

Each file name has 4 sections separated by dashes. Figure 47 shows an example of a file name and meaning of each section. The first section shows the orifice diameter, the second section shows the signal frequency, the third section shows the distance downstream of the jet along the centerline (Y value) and the last section shows the distance away from the orifice center to the East or West direction(X value).

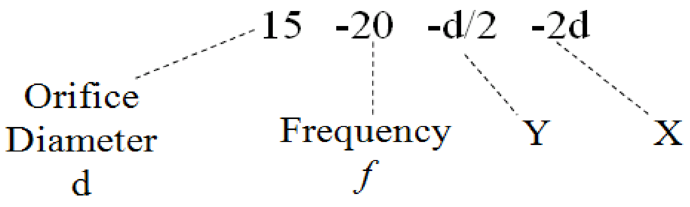

Figure 47 File name and definition of each section.

Hot-wire data can be acquired by selecting the “Trigger” on the next screen (Figure 48). A pop up window appears to enter the temperature. In all the current experiments, the temperature is considered to be at 20 °C. According to the settings 16 kilo points of data are then taken over 3.27 seconds and automatically saved on the computer hard drive. Figure 49 shows these data with synthetic jet velocities versus time in the first graph of the acquisition screen. The third graph shows the input sinusoidal signal versus time. For each of these graphs, minimum and maximum limits on the vertical axis can be configured using the “Config Graph” button (Figure 49).

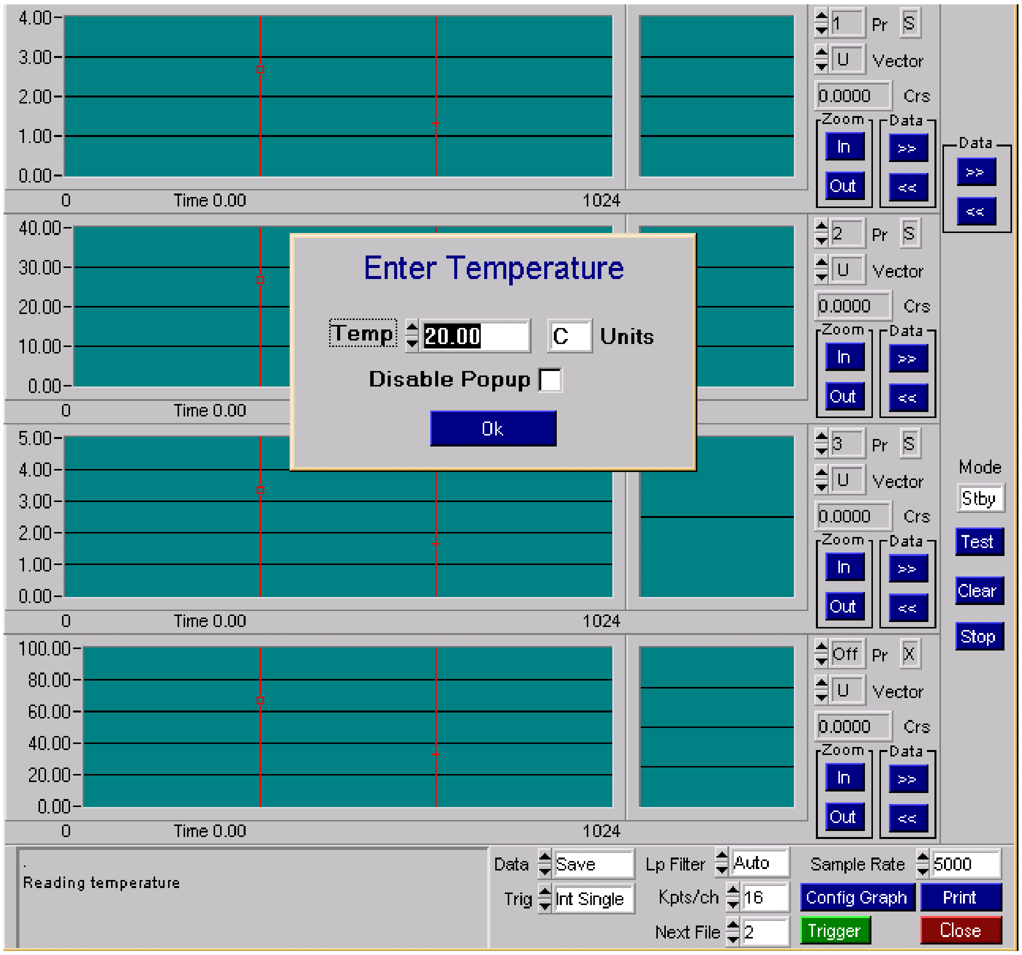

Enter Temperature

Temp 20.00 C Units

Disable Popup ☐

Reading temperature

Data Save

Trig Int Single

Lp Filter Auto

Kpts/ch 16

Next File 2

Sample Rate 5000

Mode Stby

Figure 48 Triggering temperature requirement.

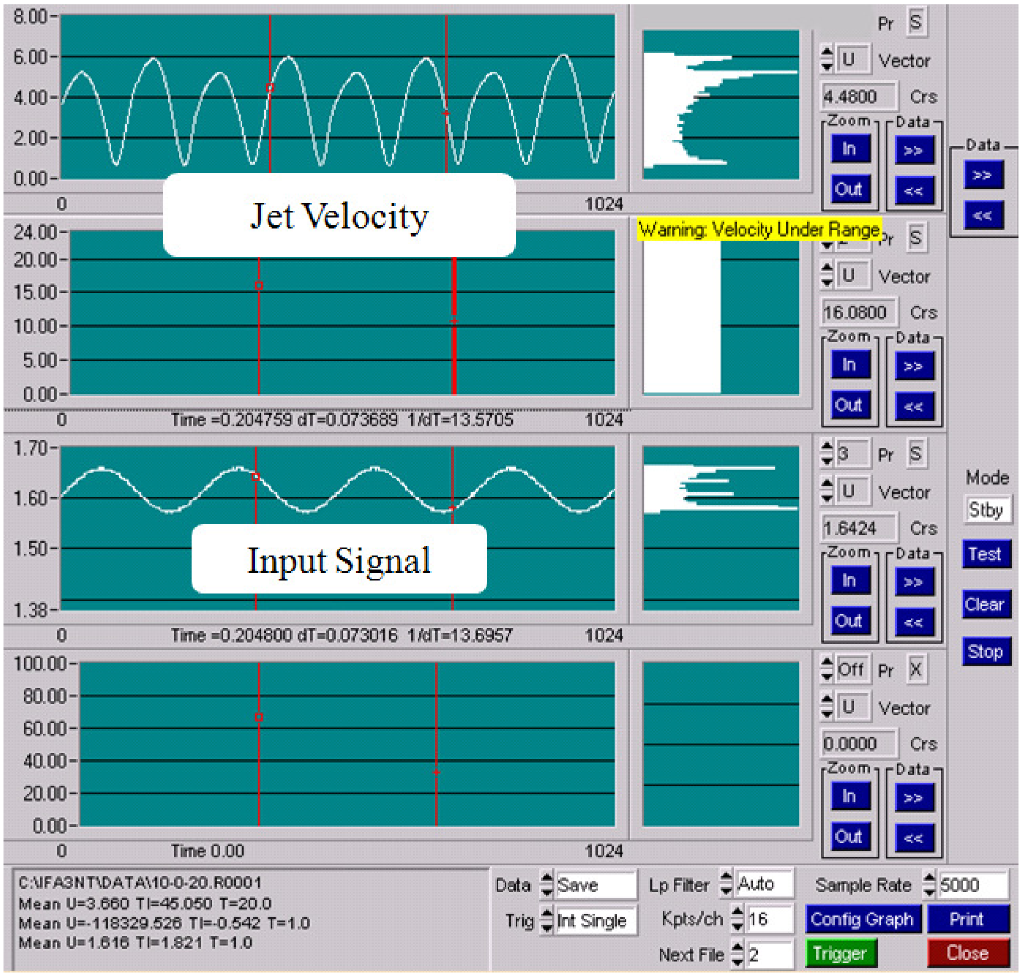

```
Time =0.204759 dT=0.073689  1/dT=13.5705
Time =0.204800 dT=0.073016  1/dT=13.6957
Time 0.00
```

Crs 4.4800

Crs 16.0800

Pr 3; Crs 1.6424

Pr Off; Crs 0.0000

```
C:\IFA3NT\DATA\10-0-20.R0001
Mean U=3.660 TI=45.050 T=20.0
Mean U=-118329.526 TI=-0.542 T=1.0
Mean U=1.616 TI=1.821 T=1.0
```

Data: Save

Trig: Int Single

Lp Filter: Auto

Kpts/ch: 16

Next File: 2

Sample Rate: 5000

Figure 49 Input signal and synthetic jet velocity graph.

B.3 Hot-wire Anemometry Post Analysis

Saved data files can then be extracted using the "Analysis-Velocity" screen. After selecting the files using the "Get File" button, text format can be chosen to extract and convert the files to a readable version for using Excel spreadsheet software (Figure 50).

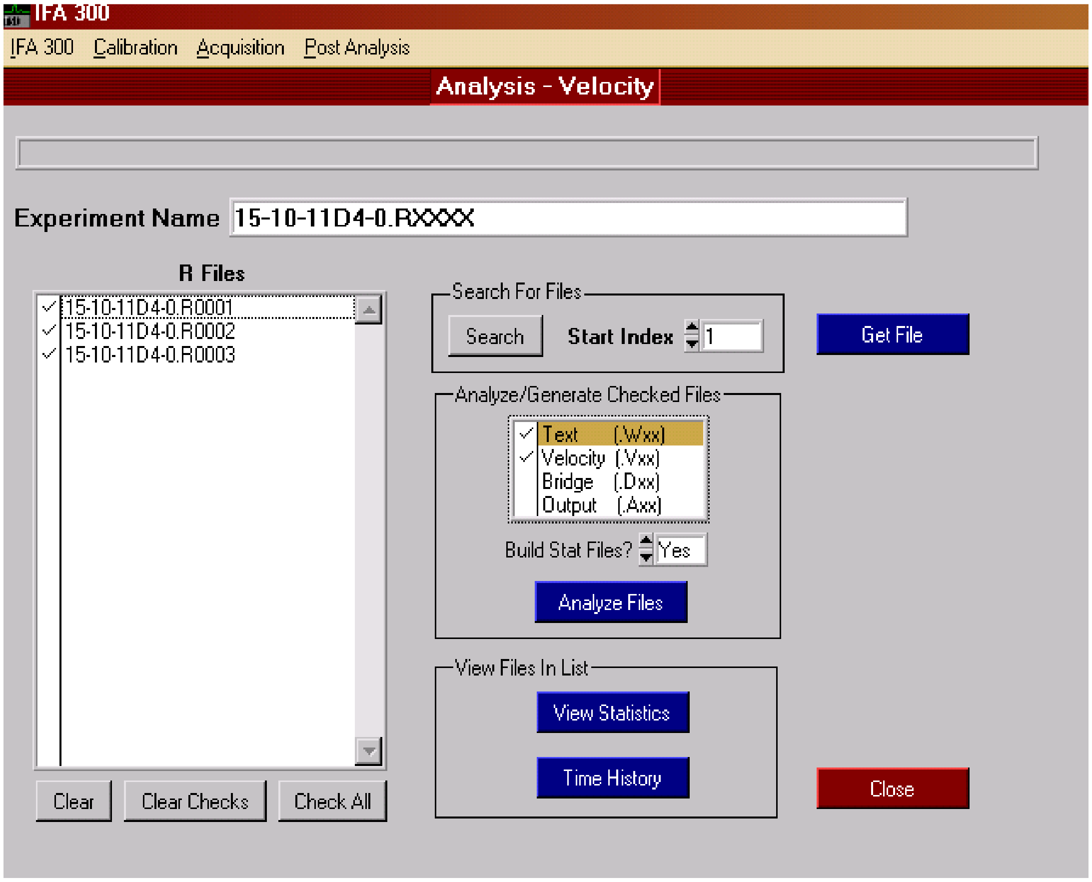

Experiment Name 15-10-11D4-0.RXXXX

R Files
- ✓ 15-10-11D4-0.R0001
- ✓ 15-10-11D4-0.R0002
- ✓ 15-10-11D4-0.R0003

Start Index 1

- ✓ Text (.Wxx)
- ✓ Velocity (.Vxx)
- Bridge (.Dxx)
- Output (.Axx)

Build Stat Files? Yes

Figure 50 Post analysis.

Appendix C: Data Obtained From the Measurements

The data for all the measurements in this study are gathered on the attached CD-ROM. The main directory according to Section 3.2 contains three folders named: Category 1, Category 2 and Category 3. Each category has two sub folders named 10 mm and 15 mm which is the diameter of the orifice. Two folders can be found under each of the subfolders named 10 Hz and 20 Hz which is the frequency of oscillations. Excel files are saved under each of these folders. See Figure 47 for meaning of file names.

REFERENCES

1. **Smith, B.L. and Swift, G.W.,** *A Comparison between Synthetic Jets and Continuous Jets.* Experiments in Fluids, 2003. **34**: p. 467-472.

2. **Utturkar, Y.,** *Numerical Investigation of Synthetic Jet Flow Fields*, Master's Thesis, 2002, Mechanical and Aerospace Engineering Department, University of Florida.

3. **James, R.D., Jacobs, J.W., and Glezer, A.,** *A Round Turbulent Jet Produced by an Oscillating Diaphragm.* Physics of Fluids, 1996. **8**(9): p. 2484-2495.

4. **Holman, R.J.,** *An Experimental Investigation of Flows from Zero-Net-Mass-Flux Actuators*, PhD Thesis, 2006, Mechanical and Aerospace Engineering Department, University of Florida.

5. **Gallas, Q., Wang, G., Papila, M., Sheplak, M., and Cattafesta, L.,** *Optimization of Synthetic Jet Actuators*, 41st Aerospace Science Meeting and Exhibit. 2003: Reno, NV.

6. **Shuster, J.M. and Smith, D.R.,** *Experimental Study of the Formation and Scaling of a Round Synthetic Jet.* Physics of Fluids, 2007. **19**: p. 1-21.

7. **Smith, B.L. and Glezer, A.,** *The Formation and Evolution of Synthetic Jets.* Physics of Fluids, 1998. **10**(9): p. 2281-2297.

8. **Smith, B.L. and Glezer, A.,** *Jet Vectoring Using Synthetic Jets.* Journal of Fluid Mechanics, 2002. **458**: p. 1-34.

9. **Smith, B.L. and Glezer, A.,** *Vectoring and Small-scale Motions Effected in Free Shear Flows Using Synthetic Jet Actuators*, 35th AIAA Aerospace Sciences Meeting. 1997: Reno, NV.

10. **Pack, L.G. and Seifert, A.,** *Periodic Excitation for Jet Vectoring and Enhanced Spreading*, 37th AIAA Aerospace Sciences Meeting. 1999: Reno, NV.

11. **Guo, D., Cary, A.W., and Agarwal, R.K.,** *Numerical Simulation of Vectoring of a Primary Jet with a Synthetic Jet.* AIAA Journal, 2003. **41**(12): p. 2364-2370.

12. **Chen, F., Yao, C., Beeler, G.B., Bryant, R.G., and Fox, R.L.,** *Development of Synthetic Jet Actuators for Active Flow Control at NASA Langley.*, AIAA Fluids 2000 Meeting. 2000: Denver, CO.

13. **Travenicek, Z. and Tesar, V.,** *Annular Synthetic Jet Used for Impinging Flow Mass-transfer.* International Journal of Heat and Mass Transfer, 2003. **46**: p. 3291-3297.

14. **Mahalingam, R., Ramingy, N., and Glezer, A.,** *Thermal Management Using Synthetic Jet Ejectors.* IEEE Transactions on Components and Packaging Technologies, 2004. **27**(3): p. 439-445.

15. **Mahalingam, R.,** *Modeling of Synthetic Jet Ejectors for Electronics Cooling*, 23rd IEEE Semi-Therm Symposium. 2007: San Jose, CA.

16. **Campbell, J.S., Black, W.Z., Glezer, A., and Hartley, J.G.,** *Thermal Management of a Laptop Computer with Synthetic Air Microjets.*, 6th Intersociety Conference on Thermal and

Thermomechanical Phenomenon in Electronic Systems. 1998: Seattle, WA.

17. **Amitay, M., Smith, B.L., and Glezer, A.,** *Aerodynamic Flow Control Using Synthetic Jet Technology*, 36th AIAA Aerospace Sciences Meeting. 1998: Reno, NV.

18. **Amitay, M., Kibens, V., Parekh, D., and Glezer, A.,** *Flow Reattachment Dynamics over a Thick Airfoil Controlled by Synthetic Jet Actuators*, 37th AIAA Aerospace Sciences Meeting. 1999: Reno, NV.

19. **Ravindran, S.S.,** *Active Control of Flow Separation over an Airfoil.* Report NASA-99-TM209838, 1999, NASA: Hampton, VA.

20. **Kiddy, J., Chen, P., and Niemczuk, J.,** *Active Flow Control Using Microelectromechanical Systems*, 41st AIAA SDM Conference. 2000: Atlanta, GA.

21. **Ingard, U. and Labate, S.,** *Acoustic Circulation Effects and the Nonlinear Impedance of Orifice.* Journal of the Acoustical Society of America, 1950. **22**: p. 211-219.

22. **Medinkov, E.P. and Novitskii, B.G.,** *Experimental Study of Intense Acoustic Streaming.* Soviets Physics - Acoustics, 1975. **21**: p. 152.

23. **Lebedeva, I.V.,** *Experimental Study of Acoustic Streaming in the Vicinity of Orifices.* Soviets Physics - Acoustics, 1980. **26**: p. 331-333.

24. **Bera, J.C., Michard, M., Grosjean, N., and Comte-Bellot, G.,** *Flow Analysis of Two-dimensional Pulsed Jets by Particle Image Velocimetry*. Experiments in Fluids, 2001. **31**(31): p. 519-532.

25. **Smith, B.L. and Swift, G.W.,** *Synthetic Jets at Large Reynolds Number and Comparison to Continuous Jets*, 31st AIAA Fluid Dynamics Conference. 2001: Anaheim, CA.

26. **Fugal, S.R., Smith, B.L., and Spall, R.E.,** *Displacement Amplitude Scaling of a Two-dimensional Synthetic Jet.* Physics of Fluids, 2005. **17**(4): p. 1-10.

27. **Fugal, S.R.,** *A Numerical Study of Oscillating Flow through a Sudden Expansion*, Master's Thesis, 2004, Mechanical and Aerospace Engineering Department, Utah State University.

28. **Crook, A. and Wood, N.J.,** *Measurements and Visualizations of Synthetic Jets*, AIAA 39th Aerospace Sciences Meeting. 2001: Reno, NV.

29. **Smith, B.L., Trautman, M.A., and Swift, G.W.,** *Controlled Interactions of Adjacent Synthetic Jets*, 37th AIAA Aerospace Sciences Meeting. 1999: Reno, NV.

30. **Cater, J.E. and Soria, J.,** *The Evolution of Round Zero-Net-Mass-Flux Jets.* Journal of Fluid Mechanics, 2002. **472**: p. 167-200.

31. **Zaman, K.B. and Milanovic, I.M.,** *Synthetic Jets in Cross-flow Part 1: Round Jets*, 16th AIAA Computational Fluid Dynamics Conference

and 33rd AIAA Fluid Dynamics Conference and Exhibit. 2003: Orlando, FL.

32. **Zaman, K.B. and Milanovic, I.M.,** *Synthetic Jets in Cross-flow Part 2: Jets from Orifices at Different Geometries*, 16th AIAA Computational Fluid Dynamics Conference and 33rd AIAA Fluid Dynamics Conference and Exhibit. 2003: Orlando, FL.

33. **Gallas, Q.,** *On the Modelling and Design of Zero-Net-Mass-Flux Actuators*, PhD Thesis, 2005, Mechanical and Aerospace Engineering Department, University of Florida.

34. **Mallinson, S.G., Hong, G., and Reizes, J.A.,** *Some Characteristics of Synthetic Jets*, 30th AIAA Fluid Dynamics Conference. 1999: Norfolk, VA.

35. **Holman, R.J., Utturkar, Y., Mittal, R., Smith, B.L., and Cattafesta, L.,** *Formation Criterion for Synthetic Jets.* AIAA Journal, 2005. **43**(10): p. 2110-2116.

36. *TSI, Model 1129 Automated Air Velocity Calibrator*, Thermal Systems Inc. 2003: Minneapolis, MN.

37. **Figliola, R.S. and Beasley, D.E.,** *Theory and Design for Mechanical Measurements*. 1991: John Wiley & Sons.

38. **Jorgensen, F.E.,** *How to Measure Turbulence with Hot-wire Anemometers*, www.dantecdynamics.com/Default.aspx?ID=456 [Accessed in April 2008], Dantec Dynamics. 2005.

VITA AUCTORIS

Hoda Eiliat was born on 23rd of August 1983 in Tehran, capital of Iran. She finished her high school education in Iran High School in 1999 in Tehran and attended her Pre-University education in 2000 in Payam School in Tehran. From there she went to University of Tehran and graduated with a Bachelor Degree in Irrigation Engineering in June 2005. Presently Mrs. Eiliat is pursuing her Master of Applied Science degree in the Department of Mechanical, Automotive and Materials Engineering in University of Windsor, Windsor, Ontario, Canada with specialization in Fluids Mechanics and expects to graduate in May 2009.